Journal of Molecular Structure 1266 (2022) 133512

Contents lists available at ScienceDirect

Journal of Molecular Structure

journal homepage: www.elsevier.com/locate/molstr

Synthesis and characterization of a series of cobalt complexes: Investigation of their efficacy as sensitizers in dye-sensitized solar cell applications

Vindhya Hegde[a], C.O. Sreekala[a,*], Naveen V. Kulkarni[b,*], Dineshchakravarthy Senthurpandi[c], Jomon Mathew[d,*]

[a] Department of Physics, Amrita Vishwa Vidyapeetham, Amritapuri 690525 Kerala, India
[b] Department of Chemistry, Amrita Vishwa Vidyapeetham, Amritapuri 690525 Kerala, India
[c] Department of Inorganic and Physical Chemistry, Indian Institute of Science, Bangalore 560012 Karnataka, India
[d] Research and Post-graduate Department of Chemistry, St. Joseph's College, Devagiri 673008 Kerala, India

ARTICLE INFO

Article history:
Received 14 March 2022
Revised 24 May 2022
Accepted 11 June 2022
Available online 12 June 2022

Key words:
Cobalt-complexes
Dye-sensitized solar cell
DFT studies
HOMO-LUMO
Power conversion efficiency
Molecular structure

ABSTRACT

A series of cobalt(II) complexes possessing diverse structural and electronic properties were prepared by using varieties of ligand systems. All the complexes were thoroughly characterized by spectral and analytical and techniques including X-ray crystallography and the molecular structures were optimized by DFT studies (M06 & B3LYP methods). The theoretical HOMO-LUMO energy gaps were compared with the optical band gap energies calculated using Tauc plot. Utility of the prepared cobalt (II/III) complexes as sensitizers in the dye-sensitized solar cell was investigated. I–V parameters of the fabricated solar cells were noted and compared with the cell made using standard N719 dye. Among the twenty-one complexes investigated, complex **C4**, comprising of bis(pyrazolyl)methane ligands exhibited highest power conversion efficiency.

1. Introduction

Performance of a dye-sensitized solar cell mainly depends on the structural and functional features of the dye-molecule, especially on the absorption spectrum, stability, molecular orbital energy levels as well as its anchoring or docking ability towards the surface of semiconductor [1–8]. Ruthenium-based dyes are found to be highly successful in DSSC applications owing to their broad band of absorption in visible range and very efficient metal-to-ligand charge transfer properties [9–12]. However, the complicated protocols involved in the construction of these dyes, as well as the economic and environmental challenges they pose, makes the quest of development of alternative metallo-dyes highly desirable [13–18]. In this context, we see a burgeoning interest in the development of environment friendly and cost-effective first row transition metal-based complex-dyes for the sensitizing applications, with zinc [19–24], copper [25–28] and iron-based [29–34] systems leading the league. On the other hand, cobalt-based complexes are extensively exploited as redox mediators/electrolytes in the DSSC applications and in effect considered as the best alternatives for the conventional iodine-based electrolytes [35–39], however, their utility as sensitizers is surprisingly underexplored [40,41]. Considering the tremendous success of the cobalt-based complexes in the several important catalytic reactions, which were believed to be accessible only with the expensive, rare earth metal complexes, it is evident that with the help of the suitable ligand edifice, it is possible to build the cobalt-based systems with the desired functional and electronic properties [42–48]. We would like to extend the same strategy for the development of highly efficient 'cobalt-based dyes' for the DSSC applications. Here in this work, varieties of simple cobalt complexes with unique molecular and electronic structures were prepared using diverse classes of the ligand systems and their efficacy as sensitizer in the solar cell applications was investigated. From the corroborative experimental and theoretical studies, a cobalt-based system with potential sensitizing applications in DSSC was identified.

* Corresponding authors.
E-mail addresses: sreekalaco@am.amrita.edu (C.O. Sreekala), naveenvkulkarni@am.amrita.edu (N.V. Kulkarni), jomonmat@gmail.com (J. Mathew).

https://doi.org/10.1016/j.molstruc.2022.133512
0022-2860/

2. Experimental

2.1. Materials and instrumentation

All the chemicals used in this work, organic and metal precursors as well as the solvents were purchased from various commercial sources, Merck, Nice Chemicals, Spectrochem and Thermo Fisher Scientific and were used after the essential purification/drying procedures. The ligands, 2,2′-bipyridine (**L1**), 1,10-phenanthroline (**L2**), di(pyridin-2-yl)methanone (**L8H**), thiocarbohydrazide (**L18H$_2$**) and diphenyl thiocarbazide (**L19H$_2$**) as well as the complex, cobalt(II) phthalocyanine (**C21**) were purchased from Merck or Thermo Fisher Scientific. Fluorine doped tin oxide (FTO) glass plates (with surface resistivity ~15Ω/cm^2) and titania paste (transparent) were obtained from Sigma Aldrich. A ELICO–CM-82 conductivity bridge was used for the molar conductivity measurements. IR spectra were recorded on a Perkin Elmer Spectrum two FT-IR instrument and UV–Visible spectral analysis was done using a Perkin Elmer LAMDA 25 instrument. NMR spectral analysis was done on a Bruker Avance NEO 500 MHz NMR spectrometer at room temperature. The magnetic susceptibility values of the complexes in solid state were measured using a Faraday balance at 25 °C, using Hg[Co(SCN)$_4$] as a standard for calibration. Cyclic voltammetry studies were carried out using a CHI 610E electrochemical workstation (CH Instruments, USA). All the prepared compounds were analyzed for carbon, hydrogen and nitrogen by Thermo Scientific Flash 2000 Organic Elemental Analyzer. Quantitative analysis of cobalt and chloride content of the complexes was done by following the established protocols [49]. Single crystal x-ray study was done using Bruker APEX-II Kappa machine. Surface analysis of the fabricated solar cell unit was carried out using a FEI Quanta FEG 200 - High Resolution Scanning Electron Microscope and Thermo Scientific - Nicolet iS50 Raman Spectrophotomenter. Kiteley 2420-A source meter and Newport solar simulator were used for the measurement of I-V characteristics and the illumination intensity was measured using a Lutron LX-101 lux meter.

2.2. Synthesis of ligands

Ligands, bis(3,5-dimethyl-1*H*-pyrazol-1-yl)methane (**L3**) [50,51] bis(1H-pyrazol-1-yl)methane (**L4**) [50], N,N'-di(pyridin-2-yl)-formimidamide (**L5H**) [52], 2,2′-(pentane-2,4-diylidene)bis-(hydrazine-1-carboxamide) (**L6H$_2$**) [53], Diphenylcarbazide (**L7H$_2$**) [54], 1,3-bis(2-pyridylimino)isoindoline (**L9H**) [55], N,N′-bis(salicylidene)−1,2-phenylenediamine (**L10H$_2$**) [56,57], N,N'-bis(salicylidene)ethylenediamine (**L11H$_2$**) [58], N,N'-bis(5-hydroxysalicylidene)ethylenediamine (**L12H$_2$**) [59,60], salicylaldoxime (**L13H$_2$**) [61], salicylideneaniline (**L14H**) [62], salicylaldehyde hydrazone (**L15H**) [63], salicylaldehyde azine (**L16H$_2$**) [64], N'-(salicylidene)hydrazinecarbothiohydrazide (**L17H$_2$**) [65] and 1, 5- bis(acetophenone) thiocarbohydrazone (**L20H$_2$**) [66,67] were prepared by following the procedures reported in literature and duly characterized by spectro-analytical methods.

Bis(3,5-dimethyl-1*H*-pyrazol-1-yl)methane (L3):

Colorless crystalline solid; Yield 92%; M.P. 104–106 °C; IR (KBr, selected, cm^{-1}) 2981 (w), 2925 (w), 1557 (s), 1463 (s), 1419 (s), 1365 (s), 1267 (s), 1139 (m), 1035 (m), 970 (m), 812 (s), 776 (s), 711 (m), 673 (s); UV–Vis (MeOH, 10^{-3} M) (λ_{max} in nm (log ε in dm^{3}mol^{-1}cm^{-1})) 226 (3.49), 255 (3.41); ^{1}H NMR ($CDCl_3$, 500 MHz, 298 K, ppm) δ 6.05 (s, 2H, C*H*pz), 5.77 (s, 2H, -C*H*$_2$-), 2.41 (s, 3H, C*H*$_3$pz), 2.18 (s, 3H, C*H*$_3$pz); ^{13}C{^{1}H} NMR ($CDCl_3$, 125 MHz, 298 K, ppm) δ 148.7 (s, 3-*C*CH$_{3pz}$), 141.1 (s, 5-*C*CH$_{3pz}$), 107.0 (s, 4-*C*H$_{pz}$), 60.8 (s, pz-*C*H$_2$-pz), 14.1 (s, 3-C*H*$_{3pz}$), 11.6 (s, 5-C*H*$_{3pz}$); Elemental Analysis for $C_{11}H_{16}N_4$, Calcd (found) C 64.68 (64.32), H 7.90 (8.02), N 27.43 (27.75)%.

Bis(1H-pyrazol-1-yl)methane (L4):

Colorless crystalline solid; Yield 90%; M.P. 107–108 °C; IR (KBr, selected, cm^{-1}) 3130 (m), 3108 (m), 1513 (s), 1434 (s), 1391 (s), 1375 (s), 1322 (w), 1272 (s), 1206 (s), 1094 (s), 1052 (s), 975 (w), 951 (s), 881 (m), 783 (s), 765 (s), 720 (s), 655 (s); UV–Vis (MeOH, 10^{-3} M) (λ_{max} in nm (log ε in dm^3 mol^{-1} cm^{-1})) 217 (3.23), 235 (3.47); ^{1}H NMR ($CDCl_3$, 500 MHz, 298 K, ppm) δ 7.62 (2H, d (J = 5 Hz), 5-C*H*$_{pz}$), 7.52 (2H, d (J = 5 Hz), 3-C*H*$_{pz}$), 6.27 (2H, s, C*H*$_2$), 6.26 (2H, t (J = 5 Hz), 4-C*H*$_{pz}$); ^{13}C{^{1}H} ($CDCl_3$, 125 MHz, 298 K, ppm) δ 139.7 (s, 3-*C*H$_{pz}$), 128.6 (s, 5-*C*H$_{pz}$), 106.0 (s, 4-*C*H$_{pz}$), 64.0 (s, *C*H$_2$); Elemental Analysis for $C_7H_8N_4$ Calcd (found) C 56.74 (57.02), H 5.44 (5.28), N 37.81 (38.22)%.

N,N'-di(pyridin-2-yl)formimidamide (L5H):

Colorless crystalline solid; Yield 80%; IR (KBr, selected, cm^{-1}) 3412 (m), 2906 (m), 1672 (s), 1631 (s), 1584 (s), 1486 (m), 1444(w), 1382 (m), 1346 (s), 1250 (w), 1167 (m), 996 (w), 770 (s), 726 (w), 626 (m); UV–Vis (MeOH, 10^{-3} M) (λ_{max} in nm (log ε in dm^3 mol^{-1} cm^{-1})) 223 (3.46), 291 (3.28); ^{1}H NMR ($CDCl_3$, 500 MHz, 298 K, ppm) δ 9.52 (1H, s, N*H*), 8.51 (2H, d (J = 10 Hz), m-C*H*$_{py}$) 8.31 (1H, s, NC*H*N), 7.62 (2H, t (J = 10 Hz), p-C*H*$_{py}$), 7.24 (2H, d (J = 10 Hz), o-C*H*$_{py}$), 6.95 (1H, t (J = 10 Hz), m-C*H*$_{py}$); ^{13}C{^{1}H} NMR ($CDCl_3$, 125 MHz, 298 K, ppm) δ 150.8 (s, N*C*N), 147.6 (s), 145.1 (s), 121.8 (s), 117.7 (s), 109.7 (s) (Aromatic); Elemental Analysis for $C_{11}H_{10}N_4$ Calcd (found) C 66.65 (66.42), H 5.09 (5.16), N 28.26 (28.48)%

2,2′-(pentane-2,4-diylidene)bis(hydrazine-1-carboxamide) (L6H$_2$):

Creamy-white crystalline solid; Yield 85%; M.P. 274–276 °C; IR (KBr, selected, cm^{-1}) 3460 (m), 1638 (s), 1603 (s), 1580 (s), 1495 (s), 1382 (s), 1276 (s), 1197 (m), 1170 (s), 888 (m), 761 (s), 682 (s); UV–Vis (MeOH, 10^{-3} M) (λ_{max} in nm (log ε in dm^3 mol^{-1} cm^{-1})) 224 (3.35), 258 (3.22); ^{1}H NMR (DMSO–d$_6$, 500 MHz, 298 K, ppm) δ 7.46 (2H, br, -N*H*–CO), 3.41 (2H, s, -CH$_2$-), 3.28 (4H, br, -N*H*$_2$), 2.01 (6H, s, -C*H*$_3$); Elemental Analysis for $C_7H_{14}N_6O_2$, Calcd (found) 39.25 (39.43), H 6.59 (6.78), N 39.23 (39.57)%

Diphenylcarbazide (L7H$_2$):

Colorless crystalline solid; Yield 92%; M.P. 172–174 °C; IR (KBr, selected, cm^{-1}) 3400 (w), 1637 (s), 1580 (s), 1494 (m), 1401 (s), 950 (s), 850 (m), 725 (s), 699 (s); UV–Vis (MeOH, 10^{-3} M) (λ_{max} in nm (log ε in dm^3 mol^{-1} cm^{-1})) 205 (3.37), 256 (2.80); ^{1}H NMR (DMSO–d$_6$, 500 MHz, 298 K, ppm) δ 8.29 (2H, br, -N*H*-pH), 7.54 (2H, br, -N*H*–CO), 7.15 (4H, m-C*H*$_{ph}$), 6.74 (4H, d (J = 10 Hz), o-C*H*$_{ph}$), 6.70 (2H, t (J = 10 Hz), p-C*H*$_{ph}$); ^{13}C{^{1}H} NMR (DMSO–d$_6$, 125 MHz, 298 K, ppm) δ 159.8 (s, >CO), 149.8 (s), 128.6 (s), 118.5 (s), 112.1 (s) (Aromatic); Elemental Analysis for $C_{13}H_{14}N_4O$, Calcd (found) C 64.45 (65.03), H 5.82 (6.10), N 23.13 (23.43)%

1,3-bis(2-pyridylimino)isoindoline (L9H):

Yellow crystalline solid; Yield 72%; M.P. 180 −182 °C; IR (KBr, selected, cm^{-1}) 3402 (m), 3200 (w), 3062 (w), 1630 (s), 1606 (w), 1582 (s), 1553 (m), 1528 (m), 1457 (s), 1429 (s), 1306 (s), 1260 (m), 1220 (s), 1142 (w), 1099 (s), 1043 (m), 794 (s), 773 (s), 690 (s); UV–Vis (MeOH, 10^{-3} M) (λ_{max} in nm (log ε in dm^3 mol^{-1} cm^{-1})) 247 (3.51), 315 (3.49), 409 (3.48); ^{1}H NMR ($CDCl_3$, 500 MHz, 298 K, ppm) δ 13.96 (1H, br, -NH), 8.60 (2H, m, o-C*H*$_{py}$), 8.07 (2H, m, C*H*$_{ind}$), 7.76 (2H, m, C*H*$_{ind}$), 7.65 (2H, m, p-C*H*$_{py}$), 7.46 (2H, d (J = 10 Hz) C*H*$_{py}$), 7.10 (2H, m, C*H*$_{py}$); ^{13}C{^{1}H} NMR ($CDCl_3$, 125 MHz, 298 K, ppm) δ 160.1 (s, *C*=N$_{py}$), 153.1 (s, C=N$_{ind}$), 148.6 (s), 139.2 (s), 135.6 (s), 132.9 (s), 123.7 (s), 123.0 (s), 121.2 (s) (Aromatic); Elemental Analysis for $C_{18}H_{13}N_5$, Calcd (found) C 72.23 (72.38), H 4.38 (4.21), N 23.40 (23.96)%

N,N′-bis(salicylidene)−1,2-phenylenediamine (L10H$_2$):

Yellow crystalline solid; Yield 90%; M.P. 162–164 °C; IR (KBr, selected, cm^{-1}) 3350 (m), 2920 (w), 1615 (s), 1580 (s), 1481 (s), 1458 (s), 1400 (m), 1277 (s), 1193 (s), 1151 (m), 911 (s), 760 (s); UV–Vis (MeOH, 10^{-3} M) (λ_{max} in nm (log ε in dm^3 mol^{-1} cm^{-1})) 218 (3.49), 275 (3.31), 331 (3.26); ^{1}H NMR ($CDCl_3$, 500 MHz, 298 K,

ppm) δ 13.05 (2H, s, -OH_{ph}), 8.64 (2H, s, *H*C=N), 7.40–7.33 (2H, m, CH_{ph}), 7.50–7.40 (6H, m, CH_{ph}), 7.25–7.23 (2H, m, CH_{ph}); 7.05 (2H, d (J = 10 Hz) CH_{ph}) 6.92 (2H, t (J = 10 Hz), CH_{ph}); $^{13}C\{^1H\}$ NMR ($CDCl_3$, 125 MHz, 298 K, ppm) δ 164.0 (s, *C* = N), 160.3 (s, -*C*OH_{ph}), 142.1 (s), 133.3 (s), 132.4 (s), 127.6 (s), 119.7 (s), 119.4 (s), 119.1 (s), 116.7 (s), (Aromatic); Elemental Analysis for $C_{20}H_{16}N_2O_2$, Calcd (found) C 75.93 (76.46), H 5.10 (5.32), N 8.86 (9.24)%

N,N'-bis(salicylidene)ethylenediamine ($L11H_2$):

Yellow crystalline solid; Yield 85%; M.P. 124–127 °C; IR (KBr, selected, cm^{-1}) 3404 (m), 2901 (w), 1636 (s), 1601 (m), 1577 (s), 1498 (s), 1461 9 s), 1419 (m), 1372 (w). 1284 (s), 1248 (w), 1150 (s), 1114 (m), 1042 (m), 1021 (s), 981 (m), 857 (s), 774 (m), 750 (s), 742 (s), 648 (m); UV–Vis (MeOH, 10^{-3} M) (λ_{max} in nm (log ε in dm^3 mol^{-1} cm^{-1})) 230 (3.49), 253 (3.48), 320 (3.23); ^1H NMR ($CDCl_3$, 500 MHz, 298 K, ppm) δ 13.20 (2H, br, -OH_{ph}), 8.36 (2H, s, -*H*C=N), 7.29 (2H, t (J = 10 Hz) CH_{ph}), 7.23 (2H, d (J = 10 Hz), CH_{ph}) 6.94 (2H, d (J = 10 Hz), CH_{ph}) 6.86 (2H, t (J = 10 Hz), CH_{ph}), 3.95 (4H, s, -CH_2–CH_2-); $^{13}C\{^1H\}$ NMR ($CDCl_3$, 125 MHz, 298 K, ppm) δ 168.2 (s, *C* = N), 161.1 (s, -*C*OH_{ph}), 132.3 (s), 131.4 (s), 118.6 (s), 116.9 (s) (Aromatic), 60.0 (s, -CH_2–*C*H_2-); Elemental Analysis for $C_{16}H_{16}N_2O_2$, Calcd (found) C 71.62 (72.03), H 6.01 (5.78), N 10.44 (10.82)%

N,N'-bis(5-hydroxysalicylidene)ethylenediamine ($L12H_2$):

Yellow-orange crystalline solid; Yield 85%; M.P. 280–282 °C; IR (KBr, selected, cm^{-1}) 3350 (m), 2910 (m), 1640 (s), 1600 (m), 1509 (m), 1455 (s), 1408 (m), 1307 (m), 1261 (s), 1220 (s), 1163 (s), 1045 (s), 862 (m), 832 (s), 792 (m); UV–Vis (MeOH, 10^{-3} M) (λ_{max} in nm (log ε in dm^3 mol^{-1} cm^{-1})) 240 (3.48), 260 (3.38), 351 (3.18); ^{1}HNMR (DMSO–d_6, 500 MHz, 298 K, ppm) δ 12.62 (2H, s, -OH_{ph}), 8.50 (2H, s, *H*C=N), 6.78 (2H, s, CH_{ph}) 6.70 (4H, m, CH_{ph}), 3.80 (4H, s, -CH_2–CH_2-); $^{13}C\{^1H\}$ NMR (DMSO–d_6, 125 MHz, 298 K, ppm) δ 168.3 (s, >*C* = N), 155.1 (s, -*C*OH_{ph}), 150.3 (s, -*C*OH_{ph}), 120.1 (s), 118.5 (s), 116.9 (s), 116.3 (s) (Aromatic), 59.4 (s, -CH_2–CH_2-); Elemental Analysis for $C_{16}H_{16}N_2O_4$, Calcd (found) C 63.99 (64.16), H 5.37 (5.18), N 9.33 (9.86)%

Salicylaldoxime ($L13H_2$):

Off-white crystalline solid; Yield 88%; M.P. 60–62 °C; IR (KBr, selected, cm^{-1}) 3399 (m), 3192 (m), 1627 (s), 1615 (s), 1591 (s), 1493 (s), 1447 (s), 1424 (s), 1360 (s), 1304 (m), 1254 (s), 1119 (w), 1037 (w), 994 (m), 900 (m), 848 (s), 751 (5), 650 (s); UV–Vis (MeOH, 10^{-3} M) (λ_{max} in nm (log ε in dm^3 mol^{-1} cm^{-1})) 231 (3.49), 260 (3.41), 308 (2.91); ^1H NMR ($CDCl_3$, 500 MHz, 298 K, ppm) δ 11.22 (1H, s, -OH_{ph}), 9.95 (1H, s, C=NO*H*), 8.32 (1H, s, *H*C=N), 6.91–7.42 (4H, m, CH_{ph}); Elemental Analysis for $C_7H_7NO_2$, Calcd (found) C 61.31 (61.94), H 5.15 (4.98), N 10.21 (10.54)%

Salicylideneaniline (L14H):

Pale-yellow crystalline solid; Yield 93%; M.P. 51–54 °C; IR (KBr, selected, cm^{-1}) 3056 (w), 1617 (s), 1591 (m), 1572 (m), 1485 (s), 1457 (m), 1319 (m), 1280 (s), 1186 (s), 1150 (s), 1074 (m), 980 (m), 918 (m), 845 (s), 756 (s), 692 (m); UV–Vis (MeOH, 10^{-3} M) (λ_{max} in nm (log ε in dm^3 mol^{-1} cm^{-1})) 238 (3.48), 266 (3.45), 338 (3.41); ^1H NMR ($CDCl_3$, 500 MHz, 298 K, ppm) δ 13.42 (1H, s, -OH_{ph}), 8.62 (1H, s, *H*C=N), 7.50–6.92 (4H, m, CH_{ph}); Elemental Analysis for $C_{13}H_{11}NO$, Calcd (found) C 79.17 (79.03), H 5.62 (5.77), N 7.10 (7.55)%

Salicylaldehyde hydrazone (L15H):

Colorless crystalline solid; M.P. 98–100 °C; IR (KBr, selected, cm^{-1}) 3468 (w), 3360 (w), 3315 (w), 1644 (s), 1602 (s), 1573 (s), 1533 (s), 1459 (s), 1374 (s), 1239 (s), 1157 (w), 1097 (s), 999 (m), 951 (m), 823 (m), 745 (s), 665(s); UV–Vis (MeOH, 10^{-3} M) (λ_{max} in nm (log ε in dm^3 mol^{-1} cm^{-1})) 210 (3.41), 241 (3.03), 308 (2.91); ^1H NMR ($CDCl_3$, 500 MHz, 298 K, ppm) δ 11.62 (1H, s, -OH_{ph}), 8.18 (1H, s, *H*C=N), 7.25–7.10 (4H, m, CH_{ph}), 6.80 (2H, br, NH2); Elemental Analysis for $C_7H_8N_2O$, Calcd (found) C 61.75 (61.78); H 5.92 (6.02), N 20.58 (21.03)%

Salicylaldehyde azine ($L16H_2$):

Yellowish-green crystalline solid; Yield 90%; M.P. 226–228 °C; IR (KBr, selected, cm^{-1}) 2848 (w), 1634 (m), 1615 (s), 1557 (s), 1488 (s), 1454 (s), 1376 (s), 1272 (s), 1198 (m), 1158 (s), 1099 (w), 930 (w), 882 (s), 750 (s), 670 (s); UV–Vis (MeOH, 10^{-3} M) (λ_{max} in nm (log ε in dm^3 mol^{-1} cm^{-1})) 220 (3.44), 293 (3.38), 336 (3.37); ^1H NMR (DMSO–d_6, 500 MHz, 298 K, ppm) δ 11.12 (2H, s, -OH_{ph}), 8.98 (2H, s, *H*C=N), 7.65 (2H, d (J = 8 Hz), CH_{ph}), 7.38–7.30 (2H, m, CH_{ph}), 6.92 (4H, t (J = 8 Hz), CH_{ph}); $^{13}C\{^1H\}$ NMR (DMSO–d_6, 125 MHz, 298 K, ppm) δ 163.2 (s, >*C* = N), 158.9 (s, -*C*OH_{ph}), 133.2 (s), 131.0 (s), 119.8 (s), 118.7 (s), 116.6 (s) (Aromatic); Elemental Analysis for $C_{14}H_{12}N_2O_2$, Calcd (found) C, 69.99 (70.23), H 5.03 (5.33), N 11.66 (11.84)%

N'-(salicylidene)hydrazinecarbothiohydrazide ($L17H_2$):

Yellow crystalline solid; Yield 78%; M.P. 200–203 °C; IR (KBr, selected, cm^{-1}) 3212 (s), 3061 (m), 1623 (s), 1576 (m), 1552 (s), 1488 (m), 1455 (m), 1356 (m), 1277 (s), 1185 (m), 1038 (w), 957 (w), 800 (s), 752 (s); UV–Vis (MeOH, 10^{-3} M) (λ_{max} in nm (log ε in dm^3 mol^{-1} cm^{-1})) 241 (3.49), 292 (3.45), 359 (3.40); ^1H NMR (DMSO–d_6, 500 MHz, 298 K, ppm) δ 11.42 (1H, s, -N*H*–CO), 9.87 (1H, s, -N*H*–CO), 9.68 (1H, s, -OH_{ph}), 8.28 (1H, s, CH_{ph}), 7.95 (2H, d (J = 8 Hz), CH_{ph}), 6.78–7.25 (3H, m, CH_{ph}), 4.86 (2H, br, -NH_2); $^{13}C\{^1H\}$ NMR (DMSO–d_6, 125 MHz, 298 K, ppm) δ 176.6 (s, >*C* = S), 157.2 (s, -*C*OH_{ph}), 140.6 (s, -C = N), 131.8 (s), 128.1 (s), 121.2 (s), 119.9 (s), 116.8 (s), (Aromatic); Elemental Analysis for $C_8H_{10}N_4OS$, Calcd (found) C 45.70 (45.58), H 4.79 (4.38), N 26.65 (26.89)%

1, 5- bis(acetophenone) thiocarbohydrazone ($L20H_2$):

Yellow crystalline solid; Yiled 72%; M.P. 187–189 °C; IR (KBr, selected, cm^{-1}) 3285 (w), 2997 (w), 1600 (w), 1537 (s), 1519 (s), 1487 (m), 1393 (s), 1310 (m), 1247 (s), 1159 (w), 1068 (m), 952 (m), 876 (m), 757 (s), 696 (s); UV–Vis (MeOH, 10^{-3} M) (λ_{max} in nm (log ε in dm^3 mol^{-1} cm^{-1})) 204 (3.37), 327 (3.35); ^1H NMR (DMSO–d_6, 500 MHz, 298 K, ppm) δ 11.02 (2H, br, -NH), 7.92 (4H, d (J = 8 Hz), CH_{ph}), 7.47 (6H, m, CH_{ph}), 2.41 (6H, s, CH_3); Elemental Analysis for $C_{17}H_{18}N_4S$, Calcd (found) C 65.78 (65.93), H 5.85 (6.08), N 18.05 (18.47)%

2.3. Synthesis of cobalt complexes

In a typical procedure, 1 or 2 mmol of the ligand was dissolved in 10 ml of methanol and added dropwise to the methanolic solution of cobalt (II) chloride hexahydrate (1 mmol) with constant stirring. The reaction mixture was stirred at room temperature or refluxed for the required time period (vide infra). The solid product obtained was filtered, washed with methanol and hexane and dried using an incandescent light bulb in air. In the cases, where there was no solid formed, the solvent was slow-evaporated and the solid obtained was washed with hexane and dried using an incandescent light bulb in air.

$[(L1)_2Co(H_2O)_2]Cl_2$ (C1)

0.312 g of **L1** and 0.237 g of $CoCl_2{\cdot}6H_2O$, 4 h stirring at RT; Isolated as a purple crystalline solid; Yield 82%; M.P. > 300 °C; Molar conductance ($\wedge_M$, MeOH, 10^{-3} M, $ohm^{-1}cm^2$ mol^{-1}) 128; IR (KBr, selected, cm^{-1}) 3401 (s), 3164 (m), 1605 (s), 1574 (m), 1493 (m), 1474 (s), 1441 (s), 3115 (m), 1248 (w), 1154 (s), 1060 (m), 1022 (s), 773 (s), 736 (s), 654 (s), 632 (m); UV–Vis (MeCN, 10^{-4} M) (λ_{max} in nm (log ε in dm^3 mol^{-1} cm^{-1})) 218 (4.20), 250 (3.70), 563 (2.50), 608 (2.54), 664 (2.66); Magnetic moment (μ_{eff}) 4.71 BM; Elemental Analysis for $C_{20}H_{20}Cl_2CoN_4O_2$, Calcd (found) C 50.23 (50.09), H 4.22 (4.13), Cl 14.83 (15.12), Co 12.32 (12.01), N 11.72 (12.21)%

$[(L2)_2Co(H_2O)_2]Cl_2$ (C2):

0.360 g of **L2** and 0.237 g of $CoCl_2{\cdot}6H_2O$, 4 h stirring at RT; Isolated as a light pink crystalline solid; Yield 78%; M.P 208–210 °C; Molar conductance ($\wedge_M$, MeOH, 10^{-3} M, $ohm^{-1}cm^2$ mol^{-1}) 132; IR (KBr, selected, cm^{-1}) 3300 (m), 3133 (w), 1626 (s), 1520 (s),

1509 (s), 1463 (s), 1444 (m), 1407 (s), 1637 (m), 1266 (s), 1097 (s), 1057 (s), 990 (s), 906 (m), 771 (s), 731 (s), 650 (m), 611 (s); UV–Vis (MeCN, 10^{-4} M) (λ_{max} in nm (log ε in dm^3 mol^{-1} cm^{-1})) 210 (4.20), 260 (3.60), 585 (2.43), 677 (2.64); Magnetic moment (μ_{eff}) 4.58 BM; Elemental Analysis for $C_{24}H_{20}Cl_2CoN_4O_2$, Calcd (found) C 54.77 (54.92), H 3.83 (3.72), Cl 13.47 (13.28), Co 11.20 (11.38), N 10.65 (10.98)%

[(L3)$CoCl_2$] (C3):

0.204 g of **L3** and 0.237 g of $CoCl_2{\cdot}6H_2O$, 4 h stirring at RT; Isolated as a blue crystalline solid; Yield 90%; M.P. 278–280 °C; Molar conductance (Λ_M, MeOH, 10^{-3} M, $ohm^{-1}cm^2$ mol^{-1}) 12; IR (KBr, selected, cm^{-1}) 3012 (m), 2960 (m), 1557 (s), 1466 (s), 1444 (m), 1391 (s), 1278 (s), 1211 (m), 1051 (s), 1001 (m), 830 (s), 808 (s), 677 (s); UV–Vis (MeCN, 10^{-4} M) (λ_{max} in nm (log ε in dm^3 mol^{-1} cm^{-1})) 237 (4.09), 289 (4.08), 582 (2.23), 677 (2.38); Magnetic moment (μ_{eff}) 4.89 BM; Elemental Analysis for $C_{11}H_{16}N_4CoCl_2$, Calcd (found) C 39.54 (39.38), H 4.83 (4.64), N 16.77 (16. 98), Cl 21.22 (21.58), Co 17.64 (17.32)%

[(L4)$_2$Co(H_2O)$_2$]Cl_2 (C4):

0.296 g of **L4** and 0.237 g of $CoCl_2{\cdot}6H_2O$, 4 h stirring at RT; Isolated as a purple-blue crystalline solid; Yield 92%; M.P. > 300 °C; Molar conductance (Λ_M, MeOH, 10^{-3} M, $ohm^{-1}cm^2$ mol^{-1}) 126; IR (KBr, selected, cm^{-1}) 3423 (s), 1632 (s), 1599 (s), 1526 (m), 1450 (s), 1400 (s), 1329 (m), 1301 (m), 1242 (m), 1230 (m), 1199 (m), 1150 (m), 1127 (m), 1031 (m), 1010 (m), 902 (s), 797 (m), 762 (s), 658 (m), 625 (m); UV–Vis (MeOH, 10^{-4} M) (λ_{max} in nm (log ε in dm^3 mol^{-1} cm^{-1})) 265 (4.25), 585 (2.32), 681 (2.47); Magnetic moment (μ_{eff}) 4.96 BM; Elemental Analysis for $C_{14}H_{20}Cl_2CoN_8O_2$, Calcd (found) C 36.38 (36.62), H 4.36 (4.28), Cl 15.34 (15.83), Co 12.75 (12.88), N 24.24 (24.68)%

[(L5H)Co(H_2O)$_3$*Cl*]Cl (C5):

0.198 g of **L5H** and 0.237 g of $CoCl_2{\cdot}6H_2O$, 4 h stirring at RT; Isolated as a green crystalline solid; Yield 80%; M.P.180–184 °C; Molar conductance (Λ_M, MeOH, 10^{-3} M, $ohm^{-1}cm^2$ mol^{-1}) 102; IR (KBr, selected, cm^{-1}) 3409 (s), 1667 (s), 1643 (s), 1562 (s), 1494 (s), 1447 (s), 1384 (m), 1333 (s), 1255 (m), 1164 (s), 1156 (s), 1054 (m), 1013 (s), 848 (s), 768 (s), 736 (m), 648 (m); UV–Vis (MeCN, 10^{-4} M) (λ_{max} in nm (log ε in dm^3 mol^{-1} cm^{-1})) 217 (4.47), 295 (4.32), 594 (2.88), 664 (3.08); Magnetic moment (μ_{eff}) 4.92 BM; Elemental Analysis for $C_{11}H_{16}Cl_2CoN_4O_3$, Calcd (found) C 34.58 (34.81), H 4.22 (4.38), Cl 18.56 (18.83), Co 15.42 (15.32), N 14.66 (14.89)%

[(L6)Co] (C6):

0.214 g of **L6H$_2$** and 0.237 g of $CoCl_2{\cdot}6H_2O$, 4 h reflux at 80 °C; Isolated as a blue crystalline solid; Yield 76%; M.P. 210–215 °C; Molar conductance (Λ_M, MeOH, 10^{-3} M, $ohm^{-1}cm^2$ mol^{-1}) 16; IR (KBr, selected, cm^{-1}) 3343 (s), 3314 (s), 2924 (w), 1568 (s), 1470 (m), 1405 (m), 1271 (m), 1164 (s), 1148 (s), 1049 (s), 1025 (w), 819 (m), 703 (m), 671 (m), 659 (m); UV–Vis (MeOH, 10^{-4} M) (λ_{max} in nm (log ε in dm^3 mol^{-1} cm^{-1})) 238 (3.46), 258 (3.44), 289 (3.38); UV–Vis (DMF, 10^{-4} M) (λ_{max} in nm (log ε in dm^3 mol^{-1} cm^{-1})) 617 (2.96); Magnetic moment (μ_{eff}) 4.68 BM; Elemental Analysis for $C_7H_{12}CoN_6O_2$, Calcd (found) C 31.01 (31.32), H 4.46 (4.23), Co 21.73 (21.39), N 31.00 (30.47)%

[L7Co(H_2O)$_2$] (C7):

0.242 g of **L7H$_2$** and 0.237 g of $CoCl_2{\cdot}6H_2O$, 4 h reflux at 80 °C; Isolated as a brown crystalline solid; Yield 81%; M.P. > 300 °C; Molar conductance (Λ_M, MeOH, 10^{-3} M, $ohm^{-1}cm^2$ mol^{-1}) 23; IR (KBr, selected, cm^{-1}) 3237 (m), 2922 (m), 2852 (m), 1628 (s), 1583 (s), 1555 (s), 1527 (m), 1487 (m), 1429 (m), 1306 (m), 1264 (s), 1292 (s), 1100 (s), 1037 (w), 876 (w), 796 (s), 775 (s), 652 (m); UV–Vis (MeOH, 10^{-4} M) (λ_{max} in nm (log ε in dm^3 mol^{-1} cm^{-1})) 243 (3.49), 393 (2.58), 465 (2.55), 694 (2.29); Magnetic moment (μ_{eff}) 4.36 BM; Elemental Analysis for $C_{13}H_{16}CoN_4O_3$, Calcd (found) C 46.58 (46.11), H 4.81 (5.18), Co 17.58 (17.42), N 16.71 (16.91)%

[{[(L8)$_2$Co]Cl}{[(L8)$_2$Co]OH}] (C8):

0.156 g of **L8H** and 0.237 g of $CoCl_2{\cdot}6H_2O$, 4 h stirring at RT; Isolated as an yellowish-orange crystalline solid; Yield 46%; M.P. 240–244 °C; Molar conductance (Λ_M, MeOH, 10^{-3} M, $ohm^{-1}cm^2$ mol^{-1}) 98; IR (KBr, selected, cm^{-1}) 3460 (s), 1605 (s), 1592 (s), 1444 (s), 1400 (m), 1308 (s), 1282 (s), 1244 (s), 1169 (s), 1092 (s), 1056 (m), 943 (s), 807 (s), 774 (s), 757 (s), 691 (s); UV–Vis (MeCN, 10^{-4} M) (λ_{max} in nm (log ε in dm^3 mol^{-1} cm^{-1})) 228 (3.59), 241 (3.49), 362 (1.80), 648 (1.56); ^{1}H NMR (DMSO–d_6, 500 MHz, 298 K, ppm) δ 8.01 (2H, br, 6-C*H*$_{py}$), 7.83 (2H, br, 4-C*H*$_{py}$), 7.65 (2H, br, 3-C*H*$_{py}$), 7.10 (2H, br, 5-C*H*$_{py}$); $^{13}C\{^1H\}$ NMR (DMSO–d_6, 125 MHz, 298 K, ppm) δ 160.7 (s, 2-C$_{py}$), 145.3 (s, 6-C$_{py}$), 135.8 (s, 4-C$_{py}$), 119.7 (s, 3-C$_{py}$), 115.1 (s, 5-C$_{py}$), 97.3 (s, *C*(py)$_2$(O)$_2$); Magnetic moment (μ_{eff}) Diamagnetic; Elemental Analysis for $C_{44}H_{37}ClCo_2N_8O_9$, Calcd (found) C 54.20 (54.68), H 3.82 (4.08), Cl 3.64 (3.21), Co 12.09 (11.89), N 11.49 (11.86)%.

[(L9)$_2$Co] (C9):

0.6 g of **L9H** and 0.237 g of $CoCl_2{\cdot}6H_2O$, 4 h reflux at 80 °C; Isolated as an orange-brown crystalline solid; Yield 74%; M.P. > 300 °C; Molar conductance (Λ_M, MeOH, 10^{-3} M, $ohm^{-1}cm^2$ mol^{-1}) 14; IR (KBr, selected, cm^{-1}) 3291 (m), 3098 (m), 1629 (s), 1611 (m), 1594 (s), 1557 (m), 1524 (s), 1487 (s), 1469 (s), 1431 (m), 1377 (s), 1308 (m), 1245 (s), 1208 (s), 1179 (s), 1151 (m), 1103 (s), 1071 (s), 1056 (s), 865 (m), 791 (s), 782 (s), 712 (s), 667 (m); 79 (s), 1151 (m), 1103 (s), 1071 (s), 1056 (s), 865 (m), 791 (s), 782 (s), 712 (s), 667 (m); UV–Vis (MeOH, 10^{-4} M) (λ_{max} in nm (log ε in dm^3 mol^{-1} cm^{-1})) 240 (4.11), 273 (3.83), 329 (3.81), 346 (3.77), 395 (3.84), 471 (3.38), 558 (2.85); Magnetic moment (μ_{eff}) 4.82 BM; Elemental Analysis for $C_{36}H_{24}CoN_{10}$, Calcd (found) C 65.96 (66.18), H 3.69 (3.58), Co 8.99 (9.32), N 21.37 (21.84)%

[(L10)Co(H_2O)] (C10):

0.316 g of **L10H$_2$** and 0.237 g of $CoCl_2{\cdot}6H_2O$, 4 h reflux at 80 °C; Isolated as an orange-brown crystalline solid; Yield 81%; M.P. 240–243 °C; Molar conductance (Λ_M, MeOH, 10^{-3} M, $ohm^{-1}cm^2$ mol^{-1}) 16; IR (KBr, selected, cm^{-1}) 3452 (s), 3010 (m), 1614 (s), 1581 (s), 1528 (s), 1489 (w), 1378 (m), 1337 (m), 1240 (w), 1189 (s), 1147 (s), 1029 (w), 927 (w), 812 (w), 743 (s), 586 (m); UV–Vis (MeCN, 10^{-4} M) (λ_{max} in nm (log ε in dm^3 mol^{-1} cm^{-1})) 254 (4.23), 300 (3.69), 401 (3.53), 458 (3.52), 652 (2.17); Magnetic moment (μ_{eff}) 2.51 BM; Elemental Analysis for $C_{20}H_{16}CoN_2O_3$, Calcd (found) C 61.39 (61.84), H 4.12 (4.64), Co 15.06 (14.86), N 7.16 (7.65)%

[(L11)Co(H_2O)] (C11):

0.268 g of **L11H$_2$** and 0.237 g of $CoCl_2{\cdot}6H_2O$, 4 h reflux at 80 °C; Isolated as a brown crystalline solid; Yield 81%; M.P. 210–213 °C; Molar conductance (Λ_M, MeOH, 10^{-3} M, $ohm^{-1}cm^2$ mol^{-1}) 20; IR (KBr, selected, cm^{-1}) 3430 (s), 3021 (m), 1633 (s), 1600 (s), 1541 (w), 1509 (w), 1470 (m), 1450 (s), 1400 (w), 1304 (m), 1202 (m), 1151 (m), 1129 (m), 1087 (w), 1033 (s), 903 (s), 797 (w), 762 (s), 659 (w), 626 (w); UV–Vis (MeCN, 10^{-4} M) (λ_{max} in nm (log ε in dm^3 mol^{-1} cm^{-1})) 218 (3.67), 248 (3.70), 382 (3.65), 580 (2.07), 660 (2.11); Magnetic moment (μ_{eff}) 2.44 BM; Elemental Analysis for $C_{16}H_{16}CoN_2O_3$, Calcd (found) C 55.99 (56.12), H 4.70 (4.83), Co 17.17 (17.63), N 8.16 (8.58)%

[(L12)Co(H_2O)] (C12):

0.300 g of **L12H$_2$** and 0.237 g of $CoCl_2{\cdot}6H_2O$, 4 h reflux at 80 °C; Isolated as a dark brown crystalline solid; Yield 80%; M.P. > 300 °C; Molar conductance (Λ_M, MeOH, 10^{-3} M, $ohm^{-1}cm^2$ mol^{-1}) 14; IR (KBr, selected, cm^{-1}) 3423 (s), 2910 (w), 1632 (s), 1598 (s), 1526 (m), 1450 (s), 1400 (m), 1351 (m), 1329 (m), 1242 (m), 1230 (m), 1199 (m), 1150 (s), 1127 (s), 1010 (m), 927 (w), 902 (s), 797 (w), 762 (s), 658 (m), 625 (m); UV–Vis (MeCN, 10^{-4} M) (λ_{max} in nm (log ε in dm^3 mol^{-1} cm^{-1})) 222 (4.06), 247 (4.09), 381 (3.14), 585 (2.07), 677 (2.11); Magnetic moment (μ_{eff}) 2.41 BM; Elemental Analysis for $C_{16}H_{16}CoN_2O_5$, Calcd (found) C 51.21 (51.48), H 4.30 (4.48), Co 15.71 (16.18), N 7.47 (7.95)%

[(L13)Co(H_2O)$_2$] (C13):

0.137 g of **L13H$_2$**, 0.237 g of $CoCl_2{\cdot}6H_2O$ and 2 drops of 25% ammonia solution, 4 h reflux at 80 °C; Isolated as a brown crystalline solid; Yield 86%; M.P. 110–113 °C; Molar conductance (Λ_M, MeOH, 10^{-3} M, ohm^{-1}cm^2 mol^{-1}) 32; IR (KBr, selected, cm^{-1}) 3400 (m), 3012 (w), 1557 (s), 1466 (s), 1444 (m), 1420 (m), 1391 (s), 1278 (s), 1231 (m), 1051 (s), 1004 (w), 830 (s), 808 (s), 654 (m); UV–Vis (MeOH, 10^{-4} M) (λ_{max} in nm (log ε in dm^3 mol^{-1} cm^{-1})) 241 (3.88), 303 (3.53), 393 (2.85), 520 (2.28); Magnetic moment (μ_{eff}) 4.32 BM; Elemental Analysis for $C_7H_9CoNO_4$, Calcd (found) C 36.54 (36.83), H 3.94 (4.18), Co 25.61 (25.83), N 6.09 (6.43)%

[(L14)$_2$Co(H_2O)$_2$] (C14):

0.394 g of **L14H** and 0.237 g of $CoCl_2{\cdot}6H_2O$, 4 h reflux at 80 °C; Isolated as a green crystalline solid; Yield 92%; M.P. 190–194 °C; Molar conductance (Λ_M, MeOH, 10^{-3} M, ohm^{-1}cm^2 mol^{-1}) 16; IR (KBr, selected, cm^{-1}) 3436 (s), 3310 (w), 1634 (s), 1615 (s), 1591 (s), 1572 (m), 1538 (s), 1485 (s), 1456 (s), 1379 (m), 1360 (m), 1282 (s), 1237 (s), 1184 (s), 1141 (s), 1117 (m), 1029 (s), 904 (s), 898 (s), 845 (s), 768 (s), 753 (s), 692 (s), 682 (s), 589 (s); UV–Vis (MeCN, 10^{-4} M) (λ_{max} in nm (log ε in dm^3 mol^{-1} cm^{-1})) 210 (4.25), 268 (4.02), 311 (3.96), 330 (3.97), 660 (2.30); Magnetic moment (μ_{eff}) 4.78 BM; Elemental Analysis for $C_{26}H_{24}CoN_2O_4$, Calcd (found) C 64.07 (64.28), H 4.96 (4.73), Co 12.09 (12.26), N 5.75 (5.98)%

[(L15)$_2$Co(H_2O)$_2$] (C15):

0.272 g of **L15H** and 0.237 g of $CoCl_2{\cdot}6H_2O$, 4 h reflux at 80 °C; Isolated as an off-brown crystalline solid; Yield 84%; M.P. >300 °C; Molar conductance (Λ_M, MeOH, 10^{-3} M, ohm^{-1}cm^2 mol^{-1}) 18; IR (KBr, selected, cm^{-1}) 3437 (s), 1630 (s), 1602 (s), 1563 (s), 1525 (s), 1486 (w), 1470 (s), 1372 (s), 1316 (s), 1242 (s), 1159 (m), 1094 (s), 1316 (s), 1242 (s), 1159 (m), 1094 (s), 1038 (m), 930 (m), 853 (s), 756 (s), 1038 (m), 930 (m), 853 (s), 756 (s), 704 (m), 687 (m), 593 (m); UV–Vis (MeOH, 10^{-4} M) (λ_{max} in nm (log ε in dm^3 mol^{-1} cm^{-1}) 247 (3.86), 389 (2.57), 411 (2.86); Magnetic moment (μ_{eff}) 4.67 BM; Elemental Analysis for $C_{14}H_{18}CoN_4O_4$, Calcd (found) C 46.04 (46.48), H 4.97 (4.68), Co 16.13 (15.87), N 15.34 (15.68)%

[(L16H)CoCl(H_2O)$_2$] (C16):

0.240 g of **L16H$_2$** and 0.237 g of $CoCl_2{\cdot}6H_2O$, 4 h reflux at 80 °C; Isolated as a light-brown crystalline solid; Yield 80%; M.P. >300 °C; Molar conductance (Λ_M, MeOH, 10^{-3} M, ohm^{-1}cm^2 mol^{-1}) 14; IR (KBr, selected, cm^{-1}) 3320 (s), 2900 (m), 1625 (s), 1594 (s0, 1518 (s), 1489 (m), 1468 (m), 1400 (s), 1353 (s), 1293 (m), 1251 (s), 1201 (s), 1157 (s), 1129 (w), 1068 (m), 1034 (m), 905 (s), 852 (m), 754 (s), 689 (s), 644 (m); UV–Vis (MeCN, 10^{-4} M) (λ_{max} in nm (log ε in dm^3 mol^{-1} cm^{-1})) 210 (3.81), 258 (3.79), 318 (3.49), 412 (3.29), 650 (2.30); Magnetic moment (μ_{eff}) 4.42 BM; Elemental Analysis for $C_{14}H_{15}CoClN_2O_4$, Calcd (found) C 45.49 (45.21), H 4.09 (4.39), Cl 9.59 (6.08), Co 15.94 (15.63), N 7.58 (7.84)%

[(L17)Co(H_2O)$_2$] (C17):

0.210 g of **L17H$_2$** and 0.237 g of $CoCl_2{\cdot}6H_2O$, 4 h reflux at 80 °C; Isolated as a brown crystalline solid; Yield 80%; M.P. >300 °C; Molar conductance (Λ_M, MeOH, 10^{-3} M, ohm^{-1}cm^2 mol^{-1}) 21; IR (KBr, selected, cm^{-1}) 3468 (s), 2910 (m), 1624 (s), 1609 (s), 1568 (m), 1543 (m), 1491 (m), 1470 (m), 1439 (s), 1396 (w), 1351 (w), 1298 (s), 1287 (s), 1204 (s), 1156 (s), 1131 (m), 1048 (m), 917 (m), 798 (s), 756 (s), 731 (s), 651 (m), 637 (m); UV–Vis (MeOH, 10^{-4} M) (λ_{max} in nm (log ε in dm^3 mol^{-1} cm^{-1}) 252 (3.91), 299 (3.63), 352 (3.50), 441 (3.25), 458 (3.26), 685 (2.15); Magnetic moment (μ_{eff}) 4.38 BM; Elemental Analysis for $C_8H_{12}CoN_4O_3S$, Calcd (found) C 31.69 (31.97), H 3.99 (4.23), Co 19.44 (19.78), N 18.48 (19.16)%

[(L18H$_2$)$_2$CoCl$_2$] (C18):

0.106 g of **L18H$_2$** and 0.237 g of $CoCl_2{\cdot}6H_2O$, 4 h stirring at RT; Isolated as a brown crystalline solid; Yield 42%; M.P. >300 °C; Molar conductance (Λ_M, MeOH, 10^{-3} M, ohm^{-1}cm^2 mol^{-1}) 23; IR (KBr, selected, cm^{-1}) 3460 (s), 3260 (s), 1637 (s), 1608 (s), 1560 (s), 1504 (s), 1302 (m), 1150 (s), 1110 (m), 975 (s), 780 (m), 752 (s), 674 (s); UV–Vis (MeOH, 10^{-4} M) (λ_{max} in nm (log ε in dm^3 mol^{-1} cm^{-1}) 224 (3.30), 262 (3.06), 286 (2.95), 385 (2.29); UV–Vis (DMF, 10^{-4} M) (λ_{max} in nm (log ε in dm^3 mol^{-1} cm^{-1})) 290 (3.07), 574 (2.47), 680 (2.69); Magnetic moment (μ_{eff}) 4.63 BM; Elemental Analysis for $C_2H_{12}Cl_2CoN_8S_2$, Calcd (found) C 7.02 (7.52), H 3.54 (3.82), Cl 20.72 (21.18), Co 17.23 (17.68), N 32.75 (33.32)

[(L19)Co(H_2O)$_2$] (C19):

0.258 g of **L19H$_2$** and 0.237 g of $CoCl_2{\cdot}6H_2O$, 4 h reflux at 80 °C; Isolated as a brown crystalline solid; Yield 80%; M.P. >300 °C; Molar conductance (Λ_M, MeOH, 10^{-3} M, ohm^{-1}cm^2 mol^{-1}) 13; IR (KBr, selected, cm^{-1}) 3468 (s), 2910 (m), 1624 (s), 1609 (s), 1568 (m), 1543 (m), 1491 (m), 1470 (m), 1439 (s), 1396 (w), 1351 (w), 1298 (s), 1287 (s), 1204 (s), 1156 (s), 1131 (m), 1048 (m), 917 (m), 798 (s), 756 (s), 731 (s), 651 (m), 637 (m); UV–Vis (MeOH, 10^{-4} M) (λ_{max} in nm (log ε in dm^3 mol^{-1} cm^{-1})) 242 (3.48), 395 (2.37), 477 (2.50), 682 (2.10); Magnetic moment (μ_{eff}) 4.24 BM; Elemental Analysis for $C_{13}H_{16}CoN_4O_2S$, C 44.45 (45.81), H 4.59 (4.86), Co 16.78 (17.12), N 15.95 (16.42)%

[(L20H)Co(H_2O)Cl] (C20):

0.310 g of **L20H$_2$** and 0.237 g of $CoCl_2{\cdot}6H_2O$, 4 h reflux at 80 °C; Isolated as a brown crystalline solid; Yield 80%; M.P. >300 °C; Molar conductance (Λ_M, MeOH, 10^{-3} M, ohm^{-1}cm^2 mol^{-1}) 18; IR (KBr, selected, cm^{-1}) 3440 (m), 2910 (m), 1633 (s), 1580 (m), 1508 (s), 1449 (s), 1351 (m), 1250 (m), 992 (s), 850 (m), 752 (m), 691 (m); UV–Vis (MeCN, 10^{-4} M) (λ_{max} in nm (log ε in dm^3 mol^{-1} cm^{-1}) 225 (3.85), 305 (3.99), 343 (3.99), 581 (1.20), 660 (1.25); Magnetic moment (μ_{eff}) 4.18 BM; Elemental Analysis for $C_{17}H_{19}ClCoN_4OS$, Calcd (found) C 48.41 (48.83), H 4.54 (4.92), Cl 8.40 (8.48), Co 13.97 (14.14), N 13.28 (13.67)%

2.4. Preparation of photoanode of the dye-sensitized solar cell

In a typical procedure, a FTO glass plate (2 cm × 2 cm) was cleaned thoroughly with distilled water, sonicated sequentially for 15, 10 and 5 min in alkaline-extran solution, isopropanol and distilled water and dried in a hot air oven for 2 h at 90 °C. Upon cooling to RT, commerical transperent TiO_2 paste was coated on a circular active area of 0.1266 cm^{-2} using doctor-blade method and the film was dried under air for about 15 min. After annealing for 10 min, the coated FTO plate was sintered in a muffle furnace at 450 °C for 30 min. FTO plate was then cooled to room temperature and used for dye-sensitization [68–71].

2.5. Preparation of electrolyte for dye-sensitized solar cell applications

The iodine based electrolyte used in this study was prepared by following the reported protocol [69] as described below. 7.98 g (30 mmol) of 1–butyl–3-methyl imidazolium iodide, 3.38 g (25 mmol) of 4-tetrabutyl-1-pyridine, 0.63 g (5 mmol) of iodine, 0.67 g (5 mmol) of lithium iodide and 0.59 g (5 mmol) of guanidium thyocyanate were dissolved in 50 ml of acetonitrile and sonicated for 10–15 min to obtain ~ 50 ml of electrolyte.

2.6. Fabrication of dye-sensitized solar cell unit

In a typical fabrication process, TiO_2 coated FTO glass plate (annealed & sintered, vide supra) was immersed in the 5 ml of dye-solution (5 mmol in methanol) overnight to sensitize the coated part. The dye-sensitized TiO_2 film was washed with methanol, air dried and used as a working electrode. A platinum sputtered (40 nm thickness) FTO glass plate was used as a counter electrode [72]. A complete dye-sensitized solar cell was made by assembling the platiunm counter electrode and a freshly made working electrode with a 25 μm thick polymer spacer with a hole. A couple of drops of electrolytes was added in the hole (sandwiching) and the photovoltaic parameters of the deivice were analysed.

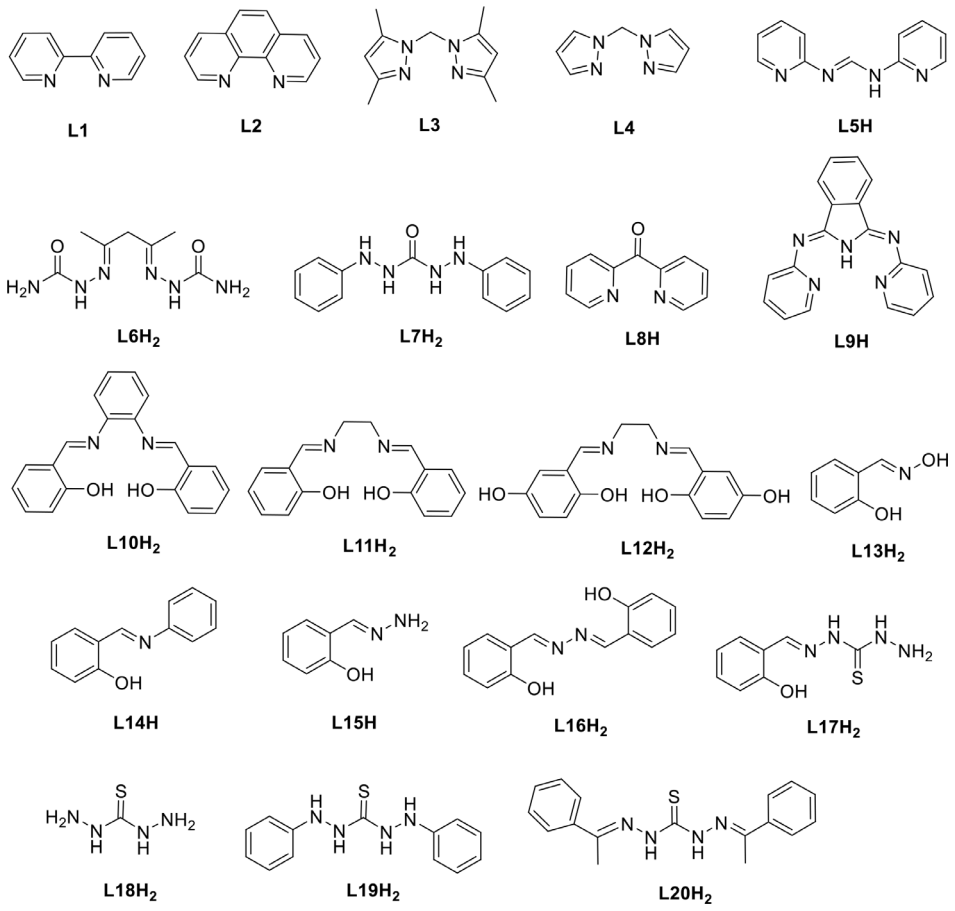

Fig. 1. Ligand systems used in this work.

2.7. X-ray crystal analysis

Pale orange tabular single crystal of complex **C4** (size 0.317 × 0.224 × 0.125 mm) and yellow tabular single crystal of complex **C8** (size 0.234 mm × 0.324 mm × 0.799 mm) were chosen under polarizing microscope for single crystal x-ray crystallographic study. The samples were taken on a nylon loop with the help of paratone oil and mounted on a diffractometer head. For **C4**: Intensity data were collected on Bruker APEX-II Ultra machine (3-Circle machine, rotating anode x-ray tube) operating at 45KV voltage and 75 mA current (for **C4**) and Bruker APEX-II Kappa machine (4-circle machine) operating at 50KV voltage and 30 mA current (for **C8**). The diffractometer was equipped with an Oxford Cyrosystem Plus Controller low temperature device for variable temperature data collection (100 K) and used MoK$_\alpha$ radiation (λ=0.71073 Å). In both the complexes, the frames were integrated with the Bruker SAINT software package using a narrow-frame algorithm [73]. Data were corrected for absorption effects using the multi-scan method (SADABS) [74]. The molecular structures were solved by dual methods using SHELXT 2014/5 [75] in the space group type $P\ -1$, with $Z = 1$ (for **C4**) $P\ -1$, with $Z = 2$ (for **C8**) and refined by full-matrix least-squares methods against F^2 by SHELXL-2018/1 [76]. All non-hydrogen atoms were refined with anisotropic displacement parameters. Hydrogen atoms bonded to the aromatic carbons were geometrical fixed by using HFIX 43 cards (riding model) and their U_{iso}'s were constrained to be 1.2 times to that of the parent carbon atoms. Hydrogen atoms bonded to the heteroatoms were found from Difference Fourier and refined with DFIX cards and their U_{iso}'s were refined. In the case of **C4**: The final anisotropic full-matrix least-squares refinement on F^2 with 132 variables converged at R1 = 2.22%, for the observed data and wR2 = 5.82% for all data. The goodness-of-fit was 1.088. The largest peak in the final difference electron density synthesis was 0.373 e-/Å^3 and the largest hole was −0.436 e-/Å^3 with an RMS deviation of 0.054 e-/Å^3. On the basis of the final model, the calculated density was 1.634 g/cm^3 and F(000), 237 e^-. In the case of **C8**: The final anisotropic full-matrix least-squares refinement on F^2 with 415 variables converged at R1 = 6.43%, for the observed data and wR2 = 21.51% for all data. The goodness-of-fit was 1.107. The largest peak in the final difference electron density synthesis was 2.774 e^-/Å^3 and the largest hole was −1.018 e^-/Å^3 with an RMS deviation of 0.186 e^-/Å^3. On the basis of the final model, the calculated density was 1.513 g/cm^3 and F(000), 646 e^-. All the crystallographic data and images provided here were generated by WinGX suite [77] and Mercury [78] programs.

2.8. Computational studies

All calculations were carried out using M06 functional [79] and B3LYP functional [80,81] methods with 6–31 G (d,p) basis set for all atoms except for cobal which was treated with relativistic SDD pseudopotential and corresponding basis set [82,83]. Gaussian 16 suite of programs was used for all calculations [84]. The solvent effects were treated with polarizable continuum model (PCM).

3. Result and discussion

3.1. Structural elucidation

All the organic ligands (Fig. 1) and the respective cobalt complexes (Fig. 2) were thoroughly characterized by molar con-

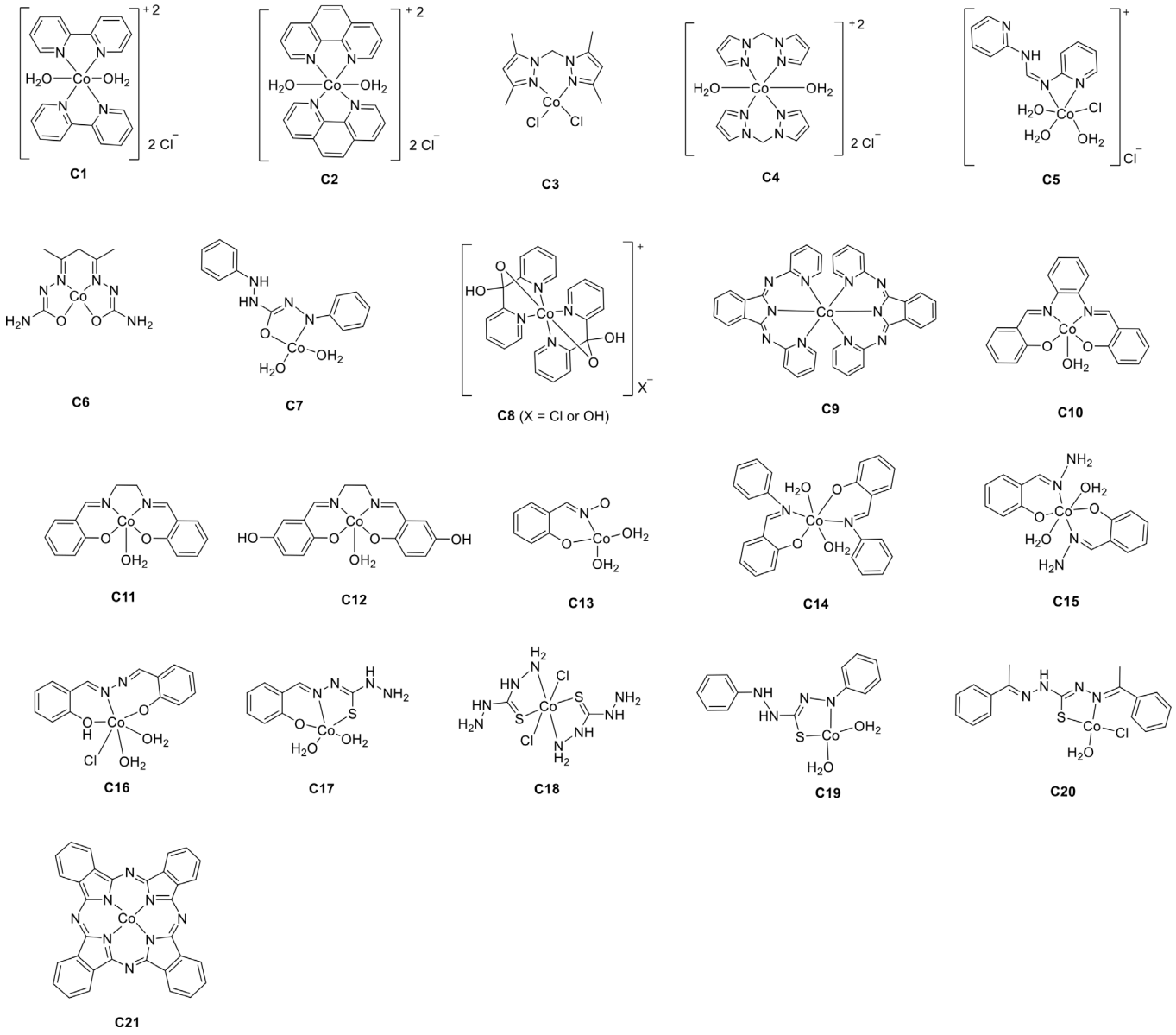

Fig. 2. Molecular structures of the cobalt complexes (C1-C21).

ductivity, magnetic moment measurement, IR, UV–Visible, NMR and mass spectral analysis as well as elemental analysis and their structure and analytical purity was determined. The characterization data of the complexes, $[(L1)_2Co(H_2O)_2]Cl_2$ (**C1**) [85], $[(L2)_2Co(H_2O)_2]Cl_2$ (**C2**) [86], $[(L3)CoCl_2]$ (**C3**) [51], [(L6)Co] (**C6**) [87], $[L7Co(H_2O)_2]$ (**C7**) [88], $[(L9)_2Co]$ (**C9**) [55], $[(L10)Co(H_2O)]$ (**C10**) [89,90], $[(L11)Co(H_2O)]$ (**C11**) [89,91], $[(L12)Co(H_2O)]$ (**C12**) [89], $[(L13)Co(H_2O)_2]$ (**C13**) [92], $[(L14)_2Co(H_2O)_2]$ (**C14**) [93], $[(L15)_2Co(H_2O)_2]$ (**C15**) [94], $[(L16H)CoCl(H_2O)_2]$ (**C16**) [95] and $[(L17)Co(H_2O)_2]$ (**C17**) [96] were compared to the reported analogues to confirm their structures. Solid state molecular structures of the complexes **C4** and **C8** were established by single crystal X-ray studies.

3.1.1. Molar conductivity measurements

The molar conductance values of all the cobalt complexes (C1-C20) were measured at room temperature in methanol solution with 10^{-3} mol/dm^3 concentration. The Λ_M values for the complexes, **C1, C2** and **C4** were found to be in the range of 126–132 ohm^{-1}cm^2 mol^{-1} and for **C5** and **C8**, in the range of 85–102 indicating the 1:2 and 1:1 electrolytic nature of the complexes respectively. While all the other complexes exhibited the Λ_M values in the range 12–32 ohm^{-1}cm^2 mol^{-1} suggesting their non-ionic nature [97–101].

3.1.2. Infrared spectroscopy studies

Infrared spectra of all the synthesized ligands and complexes were recorded using KBr pellets in the range 4000–550 cm^{-1} (see experimental section for the data). The medium intensity absorption bands observed in the range 3200–3500 cm^{-1} attributed to the -NH and/or -OH stretching vibrations (except **L3** and **L4**) [50–67]. Which in the case of complexes get broader and more intense due to the combined absorptions of the -OH stretching vibration of coordinated water molecule and -NH/-OH functionalities of the ligand backbone. Weak to medium intensity absorption bands observed around 2900–3000 cm^{-1} in all the ligands are assigned to the aromatic (phenyl and/or heterocyclic) and aliphatic -CH stretching vibrations. They remain mostly unaltered or masked under the strong -OH/-NH absorption bands in the complexes. The absorption corresponding to the azomethine group (C=N) stretch-

Table 1
Orbital energy, HOMO-LUMO band gap (computational) and optical bang gap (from UV–Visible spectral data) values of the complexes **C1-C21 (**solvent effects treated with polarizable continuum model, [†] methanol, [ǂ] acetonitrile).

Compound	M06 method			B3LYP method			Optical band gap (from UV–Visible data) (eV)
	HOMO (eV)	LUMO (eV)	LUMO–HOMO (eV)	HOMO (eV)	LUMO (eV)	LUMO–HOMO (eV)	
C1	−12.99	−7.79	5.20	−12.68	−7.92	4.76	4.62
C2	−12.49	−7.63	4.86	−12.18	−7.75	4.43	4.55
C3	−6.45	−0.96	5.48	−6.79	−0.89	5.89	4.01
C4	−13.49	−6.72	6.77	−13.07	−6.74	6.33	4.30
C4[†]	−7.97	−1.31	6.66	−7.58	−1.14	6.44	4.30
C4[ǂ]	−7.99	−1.32	6.67	−7.59	−1.15	6.44	4.30
C5	−9.47	−4.96	4.51	−9.81	−4.79	5.02	3.89
C6	−5.47	−0.55	4.92	−5.81	−0.88	4.93	4.80
C7	−4.08	−1.27	2.81	−4.38	−1.60	2.78	2.18
C8	−9.22	−4.40	4.82	−8.91	−4.55	4.36	4.42
C9	−5.74	−1.97	3.77	−5.39	−2.11	3.28	2.75
C10	−5.62	−1.89	3.73	−5.26	−2.05	3.21	3.22
C11	−5.42	−1.28	4.14	−5.06	−1.45	3.61	4.41
C12	−5.41	−1.07	4.34	−5.05	−1.26	3.79	4.38
C13	−5.52	−1.28	4.24	−5.95	−1.24	4.71	3.82
C14	−5.68	−1.79	3.88	−5.95	−1.61	4.34	3.35
C15	−5.25	−1.15	4.10	−5.41	−1.16	4.25	4.62
C16	−5.85	−2.10	3.75	−5.55	−2.24	3.31	3.50
C17	−5.05	−1.23	3.83	−5.31	−1.51	3.80	3.35
C18	−5.42	−0.65	4.78	−5.61	−0.96	4.64	4.39
C19	−4.29	−1.43	2.87	−4.61	−1.78	2.82	2.11
C20	−5.49	−1.82	3.67	−5.77	−1.58	4.19	3.10
C21	–	–	–	−4.08	−2.54	1.54	–

ing vibrations (exocyclic and/or endocyclic), observed in the range 1650–1550 cm^{-1} in the ligands, undergo significant change in the complexes, indicating the participation of azomethine groups in metal coordination. All the other characteristic absorption bands of the complexes, especially of the fingerprint region (1500–550 cm^{-1}) were found to have apparent changes in the frequency and intensity as compared to the corresponding ligands due to the steric and electronic alterations induced by metalation [51,55,85-96].

3.1.3. NMR studies

All the prepared ligands and the diamagnetic Co(III) complex, **C8** were duly characterized by the ^{1}H and ^{13}C NMR spectroscopy (except **L6H$_2$**, where we couldn't get good ^{13}C NMR spectrum due to solubility issues). The chemical shift values are referenced to solvent residue signals of $CDCl_3$ or DMSO–d6 relative to the standard $SiMe_4$ (see experimental section for the data) and compared with the literature data to confirm the molecular structures [85–96]. **C8**, exhibited only one set of signals in the ^{1}H NMR and ^{13}C NMR spectra indicating the symmetric nature of the complex [102].

3.1.4. UV–Visible spectroscopy studies

UV–Visible spectra of all the synthesized ligands (10^{-3} M, in methanol) and the corresponding cobalt (II) complexes (10^{-4} M, in acetonitrile/dimethyl formamide) were recorded in the range 200 – 900 nm and were compared with the electronic spectral data of the related compounds available in literature [50–67].

All the ligands typically exhibited two or three signals in the ranges 200–230 nm, 260–300 nm and 340–410 nm corresponding to π-π^* and n-π^* transitions mainly associated with aromatic ring, azomethine, carbonyl or thiocarbonyl groups. These peaks experience significant shift in the intensity and wavelength in the corresponding complexes due to the metal chelation. In some complexes, the ligand-metal charge transfer transitions were observed in the range 400–480 nm as medium to high intensity peaks. Complex **C1** displayed three peaks at 563, 608 and 664 nm corresponding to the D-d transitions, whereas the complexes **C2, C3, C4, C5, C11, C12, C18** and **C20** showed two peaks in the region 570–595 and 650–685 nm and the complexes **C6, C8, C9, C10, C13, C14, C16, C17** and **C19** exhibited only one peak in the 520–685 nm region. However, in the case of complexes **C7** and **C15**, no d-d transitions were observed.

The UV–Visible data of most of these complexes demonstrate absorption of light in the wavelength range of 400–480 nm, with high molar absorption coefficient values, corresponding to the charge transfer transitions and in the range 500–700 nm, with medium molar absorption coefficient values, corresponding to d-d transitions. This broader absorption range of the complex-dye molecules make them suitable candidates for the solar cell sensitizing applications [103,104].

The solution UV–Visible spectral data of the complexes was used to calculate the optical band gap of the complexes, associated with the direct allowed transitions via Tauc plot method [105,106] and the values obtained are tabulated in Table 1. Fig. 3 shows the UV–visible spectrum of complex **C4** in methanol and the corresponding Tauc plot.

3.1.5. Magnetic properties

The effective magnetic moment values (μ_{eff}) of the complexes were calculated from the corresponding room temperature magnetic susceptibility values obtained, using the formula $\mu_{eff} = 2.828(\chi mT)1/2$, where χm = molar susceptibility and T = temperature [107]. The μ_{eff} values of the complexes **C10, C11 and C12** were found to in the range 2.41–2.71 BM indicating the presence of low-spin electronic state of cobalt (II) ion [85]. On the other hand, μ_{eff} values for the tetrahedral complexes **C3, C6, C7, C13, C19** and **C20** were found to be in the range 4.18–4.89 BM [51,88,92], for the penta-coordinated systems **C9** and **C17** in the range 4.38–4.84 BM [108] and for the octahedral complexes, **C1, C2, C4, C5, C14, C15, C16** and **C18** in the range 4.42–4.96 BM [94,109]. These μ_{eff} values suggest the presence of high-spin state of the cobalt (II) ion in the corresponding complexes. Complex **C8** was found to be diamagnetic with cobalt (III) low-spin center [110]. These experimentally corroborated spin-states of the cobalt centers were considered in the DFT studies (*vide infra*).

3.1.6. Elemental analysis

The carbon, hydrogen, nitrogen, cobalt and chloride analysis data were found to be in best agreement with the proposed empirical formulae of the prepared ligands and complexes (Fig. 1 and

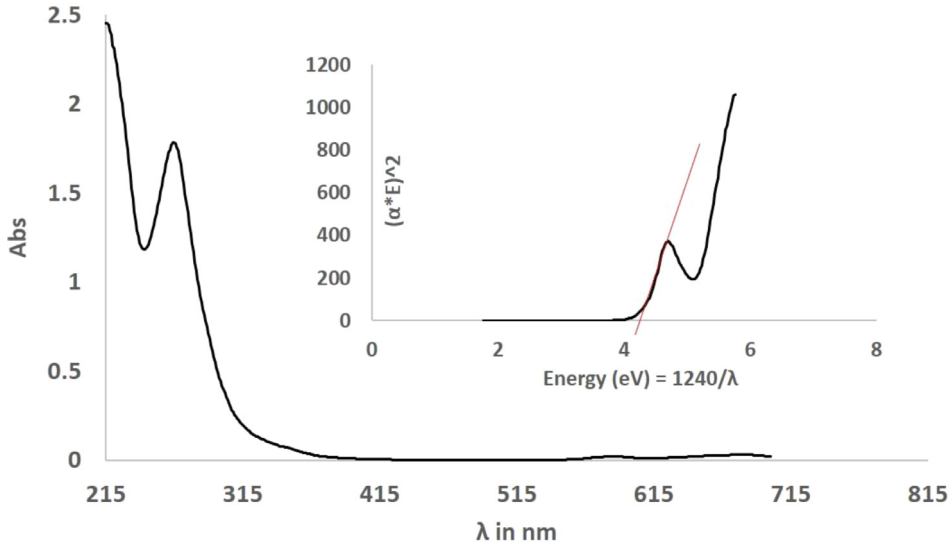

Fig. 3. UV-visible spectrum of complex **C4** in acetonitrile and the corresponding Tauc plot.

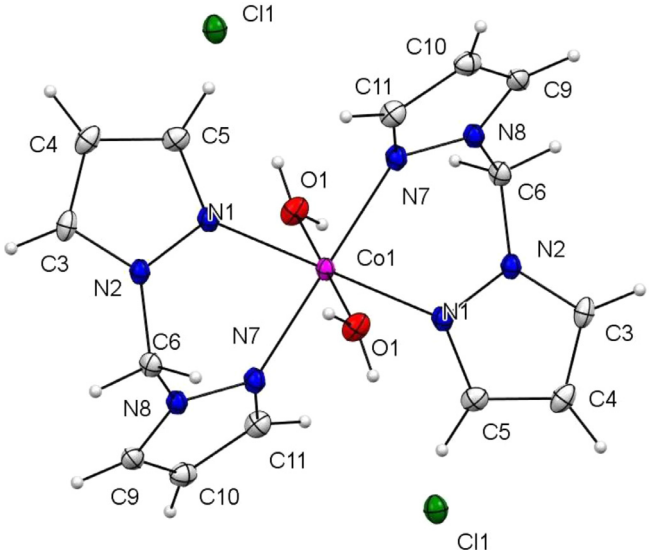

Fig. 4. Molecular structure of the complex **C4** (ORTEP diagram - thermal ellipsoids set at 50% probability). Selected bond lengths and angles: Co1-O1= 2.1069(10), Co1-N1 = 2.1135(11), Co1-N7 = 2.1269(11) Å. O1-Co1-N1 = 90.85(4), O1-Co1-N7 = 88.22(4), N1-Co1-N7 = 92.02(4), N7-Co1-N7$^{\#}$ = 180.0, N1-Co1-N1$^{\#}$ = 180.0°.

Fig. 2) and therefore confirm the analytical purity of the compounds.

3.1.7. X-ray diffraction studies

A perspective view of the molecular structure of the complex **C4** along with the details of the selected bond lengths and angles is depicted in Fig. 4. Asymmetric unit contains one molecule of ligand **L4**, one coordinated water molecule and one chloride ion. The main cationic complex is consisting of a N_4O_2 coordinated Co(II) species, having a slightly distorted octahedral geometry with the two bis(pyrazolyl) ligand (**L4**) moieties binding in a bidentate mode *via* pyrazole nitrogen atoms. The corresponding Co-N bonds of the two trans-seated ligands are found to be the same indicating the symmetric nature of the complex, however the Co-N bonds of the same ligand are slightly different (viz. Co1-N1 = 2.1135(11) and Co1-N7 = 2.1269(11) Å). The bite angle of the bidentate ligand (viz. N1-Co1-N7 = 92.02(4)°) is found to be slightly wider than that of the cobalt complex **C3** bearing the corresponding methyl substituted ligand [51] and a copper complex bearing the same ligand [111]. Both the ligands form a characteristic, boat like, six membered metallocycles (viz. N1-N2-C6-N8-N7-Co1) with a dihedral angles between the planes (indicator of depth of the boat), N1,N2,N8,N7/N2,C6,N8 = 125° and N1,N2,N8,N7/N1,Co1,N7 = 164° [51,101]

Hydrogen bonding interactions between the chloride counter ions, coordinated water molecules and hydrogen atoms of the pyrazole ring motif are found to lead to formation of a three-dimensional network in the crystal structure (Fig. 5).

The solid-state structure of the cobalt complex **C8** was derived from the X-ray diffraction data. The asymmetric unit contains two cationic molecues, one chloride ion, one hydroxy ion and six water molecules. A perspective view of the molecular structure of the main cationic complex along with the details of the selected bond lengths and angles is depicted in Fig. 6. The main cationic complex is consisting of a N_4O_2 coordinated Co(III) species, having a slightly distorted octahedral geometry with the two hydrated ligand moieties binding in a mono-anionic, tridentate mode. Similar to the earlier observations, the monoanionic ligand is found to stabilize the high oxidation state of the cobalt center (viz, +3), with the help of strong σ-donor oxygen atom [112–116]. Charge on the Co(III) is neutralized by two deprotonated hydroxyl groups of the hydrated ligand **L8** and a counter chloride or hydroxide anion [112–116]. The equatorial Co-N bond (viz. Co(1) – N(15) = 1.918(3) Å) is found to be longer than the axial Co-O bond (Co1 – O8 = 1.881(2) Å). The trans-coordinated pyridyl rings as well as the oxygen atoms are found to be perfectly linear as the metal ion sits on special position −1 (∠ N1$^{\#}$ – Co1 – N1 = ∠ O8 – Co1 – O8$^{\#1}$ = ∠ N15 – Co1 – N15$^{\#1}$ = 180.0 °). The two puckered five-membered metallocycles formed upon chelation have the dihedral angles ∠Co1 – N15 – C10 – C7 = −2.98° and ∠Co1 – N1 – C6 – C7 = 3.67°. Hydrogen bonding interactions among the chloride and hydroxide anions, coordinated oxygen atom and uncoordinated hydroxy group of the ligand motif as well as the solvated water molecules, led to the formation of a three-dimensional network, which stabilizes the crystal structure (Fig. 7).

3.2. HOMO-LUMO gaps from dft studies

From the DFT optimized molecular structures (see experimental section for the details, Cartesian coordinates of the optimized structures are provided in SI), the orbital energies and HOMO

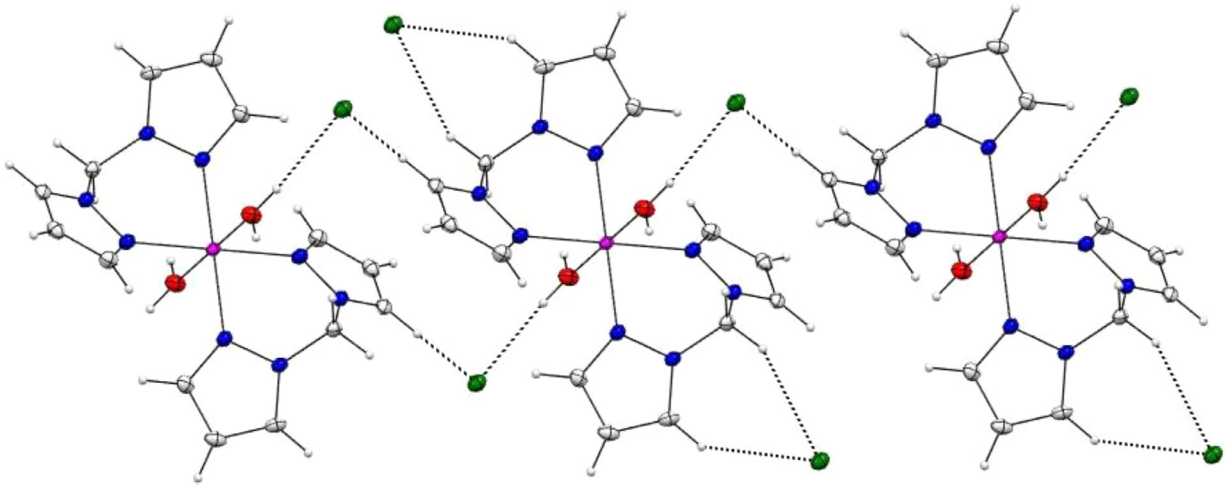

Fig. 5. ORTEP diagram portraying three-dimensional hydrogen bonding network formation in **C4** structure (thermal ellipsoids set at 50% probability; atomic color codes: gray – carbon, blue – nitrogen, red – oxygen, green – chlorine, mangenta – cobalt; projected hydrogen bond distances (bold dotted lines) are < 2.70 Å; only relevant molecules are shown). (For interpretation of the references to colour in this figure legend, the reader is referred to the web version of this article.)

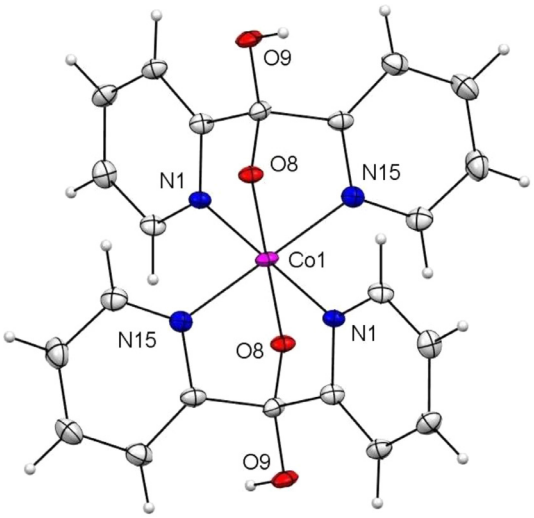

Fig. 6. Molecular structure of the main cationic complex **C8** (ORTEP diagram - thermal ellipsoids set at 50% probability; counter anion and solvent molecules are removed for the clarity). Selected bond lengths and angles: Co1 – O8 = 1.881(2), Co1 – N15 = 1.918(3), Co1 – N1 = 1.919(3) Å. O8 – Co1 – O8$^{\#}$ = 180.0, O8 – Co1 – N15 = 96.77(12), O8$^{\#}$ – Co1 – N15 = 83.23(12), O8 – Co1 – N15$^{\#}$ = 83.23(12), O8_1$^{\#}$ – Co1_1 – N15$^{\#}$ = 96.77(12), N(15) – Co1 – N15$^{\#}$ = 180.0, O8 – Co1 – N1$^{\#}$ = 96.79(11), O8$^{\#}$ – Co1 – N1$^{\#}$ = 83.21(11), N15 – Co1 – N1$^{\#}$ = 88.51(13), N15$^{\#}$ – Co1 – N1$^{\#}$ = 91.49(13), O8 – Co1 – N1 = 83.21(11)^{o}.

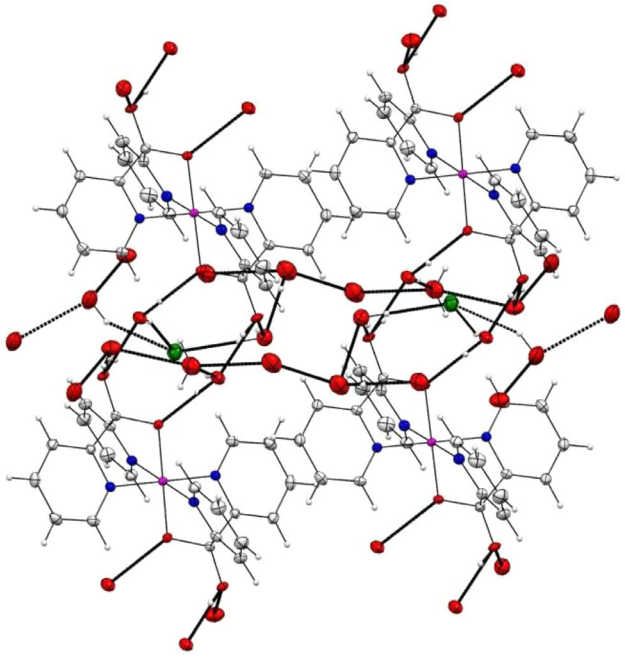

Fig. 7. ORTEP diagram portraying three-dimensional hydrogen bonding network formation in **C8** structure (thermal ellipsoids set at 50% probability; atomic color codes: gray – carbon, blue – nitrogen, red – oxygen, green – chlorine, mangenta – cobalt; projected hydrogen bond distances (bold dotted lines) are < 3.00 Å; only relevant molecules are shown). (For interpretation of the references to colour in this figure legend, the reader is referred to the web version of this article.)

(highest occupied molecular orbitals) - LUMO (lowest occupied molecular orbitals) energy gap of the complexes were calculated and are presented in the Table 1. Interestingly, both the theoretical methods provided similar values of the orbital energies and HOMO-LUMO band gaps indicating the linear correlation between the two methods used. These computational values were also found to be comparable with the optical bandgap values of all the complex-dyes, obtained from the Tauc plot analysis (vide supra) [117–119].

For an ideal dye sensitizer, in order to facilitate the electrons injection to the conduction band of semiconducting metal oxide as well as to regain electrons from redox-electrolyte solution, HOMO energy levels must be below the HOMO energy level of the electrolyte and the LUMO energy levels should have higher energy than that of the conduction band of the semi-conducting metal oxide. It can be observed from Table 1 that the HOMO energy levels of all the cobalt complexes, except **C7** and **C19**, are sufficiently lower than the redox potential of the iodide/triiodide electrolyte (i.e., −4.9 eV), indicating that the reduction of dye-molecules can be efficiently achieved by the oxidation of electrolyte in the process. On the other hand, The LUMO energy levels of all the synthesized metallo-dye molecules are higher than the conduction band of TiO_2 (i.e., −4.0 eV), indicating the high prospects for effective electron injection from the excited state of the dye molecules to the conduction band of the semiconductor. In the case of complexes **C1, C2, C4, C5** and **C8** the LUMO energy levels were found to be slightly lower than that of the TiO_2 [120]. However, when the solvent effects of acetonitrile and methanol in the case of **C4** were

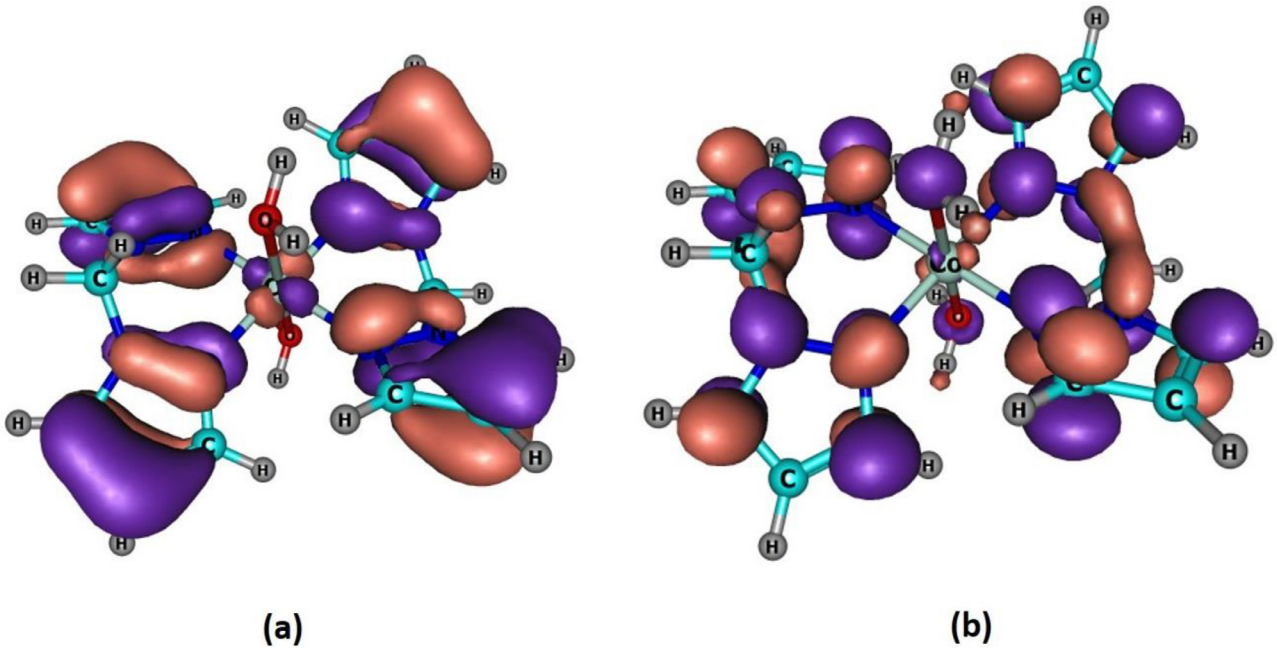

Fig. 8. DFT optimized structure of complex **C4** portraying (a) spatial distribution of HOMOs and (b) distribution of LUMOs.

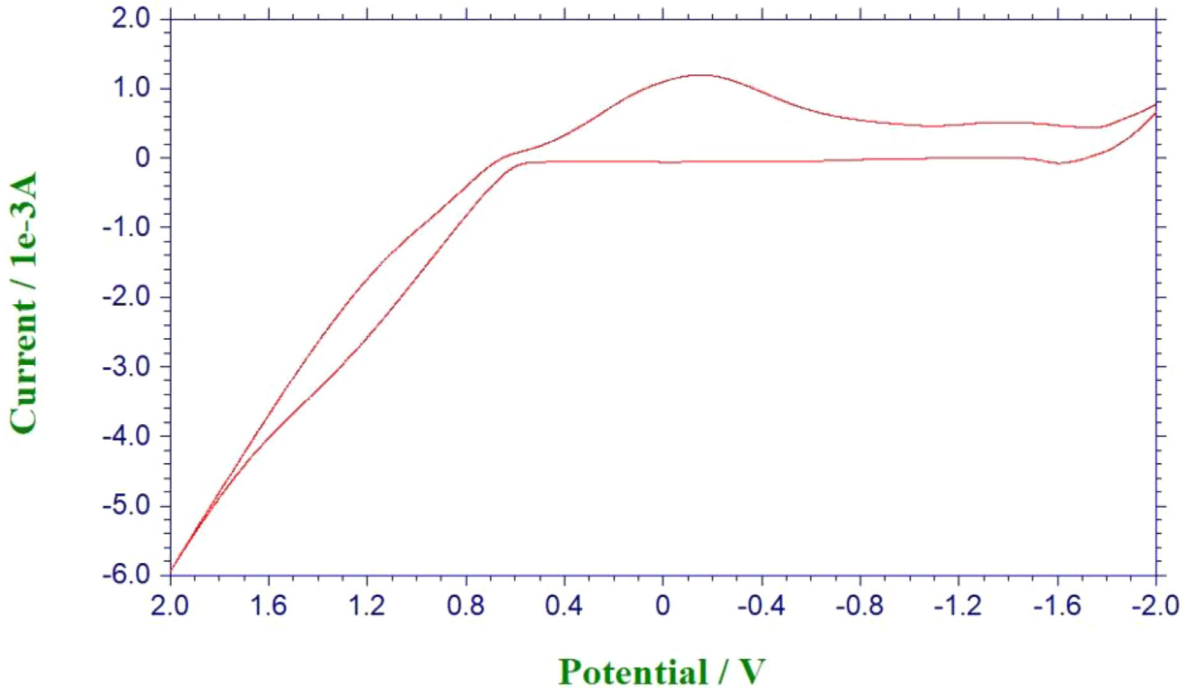

Fig. 9. Cyclic voltammogram of complex **C4** measured in DMSO at the scan rate of 0.1 V/s. (For interpretation of the references to colour in this figure legend, the reader is referred to the web version of this article.)

considered and treated with polarizable continuum model (PCM), a drastic change in their HOMO and LUMO energy levels was observed. The new values were found to better fit the requirement of the good sensitizer. Fig. 8 portrays the spatial distribution of HOMO and LUMOs in complex **C4**.

3.3. Cyclic voltammetry study of complex C4

Cyclic voltammetry study of complex **C4** (10^{-3} M, in DMSO) was carried out at room temperature using a three-electrode assembly of pencil graphite (0.7 mm fine lead, working electrode), platinum (auxiliary electrode), and aqueous Ag^{+}/AgCl reference electrode. Benzyltriethylammonium bromide (0.1 M) was used as supporting electrolyte. Voltammogram of the cobalt complex **C4** recorded in DMSO, in the range −2.0 V to 2.0 V at the scan rate of 0.1 V/s is depicted in Fig. 9.

Complex **C4** exhibits a single anodic peak at −1.61 V corresponding to Co(II) → Co(III) oxidation. During the reverse scan two cathodic peaks were observed, at −1.40 and −0.15 V corresponding to the reduction reactions. The molecular orbital energy levels and energy band gap are calculated using the empirical relations E_{HOMO} = [(E_{ox} - E_{fer} + 4.8] eV and E_{LUMO} = E_{HOMO} + E_g, where

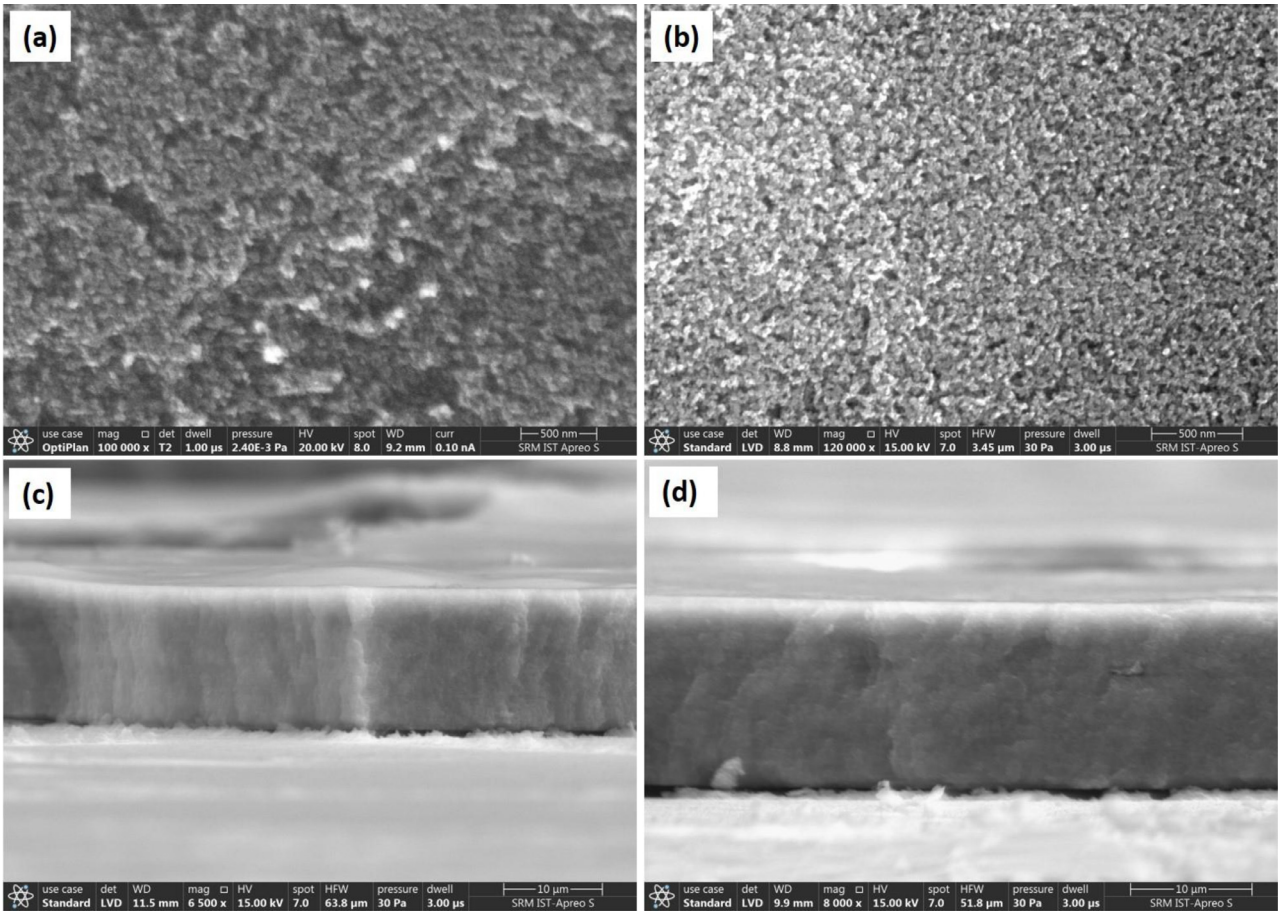

Fig. 10. SEM image of TiO_2 layer on the FTO glass plate, (a) after annealing and (b) after sensitizing with the complex **C4**; FESEM cross-section image of TiO_2 layer on the FTO glass plate, (c) after annealing and (d) after sensitizing with the complex **C4**.

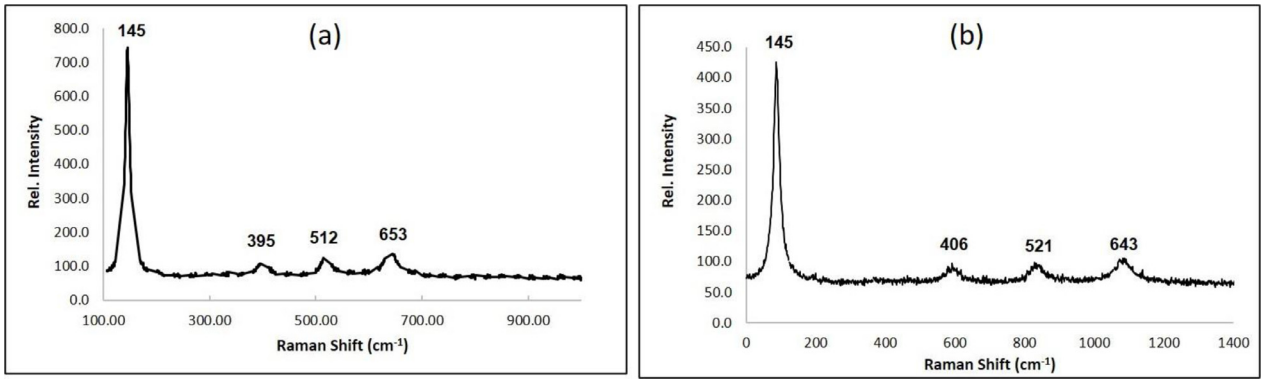

Fig. 11. Raman spectra of TiO_2 layer on the FTO glass plate(a) after annealing and (b) after sensitizing with the complex **C4.**

E_{HOMO} and E_{LUMO} are the HOMO and LUMO energy levels, E_{ox} and E_{red} are the oxidation and reduction potentials of the complex respectively, E_g is the optical bandgap (obtained from UV-visible studies), 4.8 is the reference energy level of ferrocene and E_{fer} is the redox potential value of ferrocene couple measured vs. Ag/AgCl (= 0.38 eV) [121]. Based on the above equations, the HOMO and LUMO levels of the complex **C4** are calculated to be −2.81 eV and −1.49 eV respectively.

3.4. SEM and raman analysis

The surface morphology and cross-sectional analysis of the TiO_2 coated FTO glass plate was performed using a scanning electron microscope. The respective SEM images of TiO_2 coated FTO plate after annealing (Fig. 10a and 10c) and after dye-sensitizing with complex **C4** (Fig. 10b and 10d) are portrayed. Homogeneous distribution of TiO_2 particles of the same grain size (average particle size 20 nm) can be observed. Thickness of the TiO_2 coat was found to be around 14 µm, which is well within the optimal range used in DSS cells [122,123]. The Raman spectrum of the TiO_2 coated FTO plate (Fig. 11a) exhibited four characteristic peaks at 145, 395, 512 and 653 corresponding to the Raman active modes of pure anatase form of TiO_2 with symmetries, E_g, B_{1g}, A_{1g} and E_g respectively [124,125]. Significant decrease in the intensity and shifts observed in the Raman bands of TiO_2 upon dye-sensitization (Fig. 11b) are attributed to the pronounced

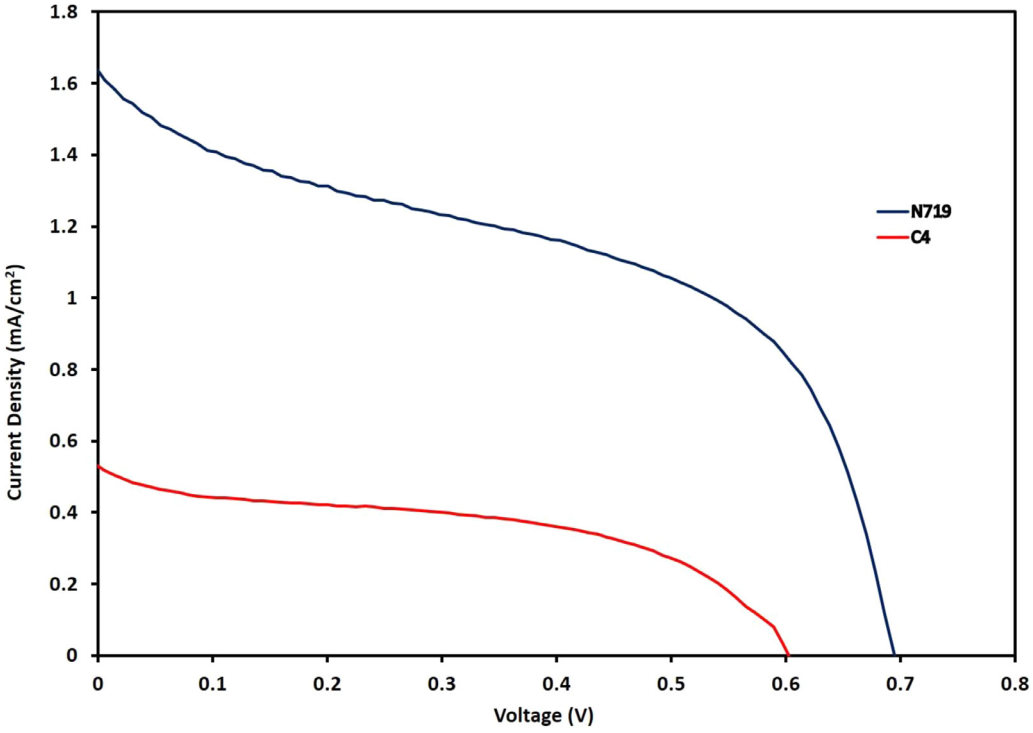

Fig. 12. I–V curves of complex **C4** (green) and standard N719 dye (blue). (For interpretation of the references to colour in this figure legend, the reader is referred to the web version of this article.)

Table 2
Experimental J-V characteristic values of complexes C1-C21*.

Sl No.	Complex-dye	Voc(V)	Jsc(mA/cm^2)	FF	PCE (%)
1	C1	0.39	0.14	38.38	0.044
2	C2	0.38	0.13	48.10	0.048
3	C3	0.25	0.11	26.83	0.014
4	C4	0.60	0.52	47.64	0.294
5	C5	0.43	0.36	44.19	0.135
6	C6	0.38	0.12	30.54	0.027
7	C7	0.25	0.09	30.90	0.083
8	C8	0.20	0.75	27.20	0.008
9	C9	0.24	0.80	30.67	0.120
10	C10	0.33	0.10	27.10	0.018
11	C11	0.29	0.05	27.01	0.009
12	C12	0.26	0.05	33.90	0.008
13	C13	0.25	0.06	38.77	0.012
14	C14	0.36	0.11	38.60	0.030
15	C15	0.14	0.22	29.04	0.017
16	C16	0.38	0.09	30.20	0.019
17	C17	0.25	0.08	35.60	0.015
18	C18	0.35	0.19	23.40	0.030
19	C19	0.14	0.09	33.16	0.009
20	C20	0.29	0.11	22.03	0.012
21	C21	0.21	0.06	27.12	0.008
22	N719	0.69	1.60	48.04	1.073

* Average of at least three experimental values.

interaction between the TiO_2 and the complex-dye molecule **C4** [126,127].

3.5. Dye sensitized solar cell devices power conversion efficiency studies

All the complexes (**C1**-**C21**) were employed as dyes (in methanol) for the fabrication of dye-sensitized solar cell units and their performance was evaluated by comparing their power conversion efficiency (PCE) obtained from the respective Current density – Voltage (I–V) curves [128]. The solar cell parameters were measured under illumination with 50 mW cm^{-2} (0.5 SUN) tungsten lamp and the corresponding I–V characteristic values of the complex-dyes are presented in Table 2. Among the twenty one cobalt complex systems investigated, three systems constituting of bis(1H-pyrazol-1-yl)methane ligand (**C4**, entry 4 in Table 2), N,N'-di(pyridin-2-yl)formimidamide ligand (**C5**, entry 5 in Table 2) and 1,3-bis(2-pyridylimino)isoindoline ligand systems (**C9**, entry 9 in Table 2) exhibited comparatively better power conversion efficiency. It is interesting to note that, the solar cell unit sensitized with complex **C4** exhibited the power conversion efficiency of 0.294%, which is about one fourth of the efficiency of the solar cell fabricated using the standard N719 dye under our optimized conditions (entry 22, Table 2) (See Fig. 12). The corresponding Voc and fill factor values of this system are also comparable with the N719-device. We are currently trying to understand the working mechanism of these devices using theoretical and high-end experimental techniques. Further attempts to improve the solar cell performance by tuning the molecular and electronic structure the cobalt-based photosensitizer **C4** are currently undergoing in our laboratory.

4. Conclusion

A series of cobalt-based complex-dye molecules comprising of varieties of ligand systems were synthesized and dully characterized by spectro-analytical techniques. From the DFT (M06 & B3LYP functional methods) optimized molecular structures, the HOMO-LUMO energy levels and electronic band gaps of all the complexes were calculated and compared with the optical band-gap values obtained by the UV–Visible spectral data (and electrochemical band-gap values in the case of **C4**). Among the twenty-one compounds investigated in this work, a complex bearing bis(pyrazolyl)methane ligand system (**C4**) was found to exhibit higher power conversion efficiency, which is about 27% of the standard N719 dye under our fabrication conditions. The Raman analysis of the Dye-sensitized TiO_2 indicated a distinct interaction be-

tween the TiO_2 and dye-molecule. Detailed studies are necessary to understand the mechanism of action of this cobalt-based solar cell sensitizer and to strategically tune its structural and electronic features to enhance its ability.

Declaration of Competing Interest

Here with we declare that there are no known competing financial interests or personal relationships that could influence the work reported in this paper.

CRediT authorship contribution statement

Vindhya Hegde: Formal analysis, Investigation, Methodology, Data curation, Writing – original draft. **C.O. Sreekala:** Resources, Supervision, Writing – review & editing. **Naveen V. Kulkarni:** Conceptualization, Formal analysis, Investigation, Data curation, Funding acquisition, Methodology, Project administration, Resources, Supervision, Validation, Visualization, Writing – original draft, Writing – review & editing. **Dineshchakravarthy Senthurpandi:** Investigation, Data curation, Validation. **Jomon Mathew:** Investigation, Data curation, Funding acquisition, Methodology, Project administration, Resources, Supervision, Validation, Writing – original draft, Writing – review & editing.

Acknowledgements

We would like to thank Dr. Animesh Das (Indian Institute of Technology Guwahati) and Dr. Kamlesh Kumar (Banaras Hindu University, Varanasi) for their help in the characterization of the compounds. **VH** thanks Amrita Vishwa Vidyapeetham for the Ph.D. fellowship. **NVK** acknowledges Science and Engineering Research Board (SERB) India for the TARE grant (TAR/2018/000881) and Prof. A. G. Samuelson, Indian Institute of Science, Bengaluru for his support.

Supplementary materials

Supplementary material associated with this article can be found, in the online version, at doi:10.1016/j.molstruc.2022.133512.

References

[1] A. Hagfeldt, G. Boschloo, L. Sun, L. Kloo, H. Pettersson, Dye-sensitized solar cells, Chem. Rev. 110 (11) (2010) 6595–6663.
[2] C.A. Bignozzi, R. Argazzi, R. Boaretto, E. Busatto, S. Carli, F. Ronconi, S. Caramori, The role of transition metal complexes in dye sensitized solar devices, Coord. Chem. Rev. 257 (2013) 1472–1492 9-10.
[3] K. Sharma, V. Sharma, S.S. Sharma, Dye-sensitized solar cells: fundamentals and current status, Nanoscale Res. Lett. 13 (2018) 381, doi:10.1186/s11671-018-2760-6.
[4] A. Carella, F. Borbone, R. Centore, Research progress on photosensitizers for DSSC front, Chem. 6 (2018) 481, doi:10.3389/fchem.2018.00481.
[5] S.-.H. Nam, K.H. Lee, J.-.H. Yu, J.-.H. Boo, Review of the development of dyes for dye-sensitized solar cells, Appl. Sci and Converg. Technol 28 (6) (2019) 194–206.
[6] S. Li, J. He, H. Jiang, S. Mei, Z. Hu, X. Kong, M. Yang, Y. Wu, S. Zhang, H. Tan, Comparative studies on the structure-performance relationships of phenothiazine-based organic dyes for dye-sensitized solar cells, ACS Omega 6 (10) (2021) 6817–6823.
[7] R. Baby, P.D. Nixon, N. Manoj Kumar, M.S.P. Subathra, N. Ananthi, A comprehensive review of dye-sensitized solar cell optimal fabrication conditions, natural dye selection, and application-based future perspectives, Environ. Sci. Pollut. Res. 29 (1) (2021) 371–404.
[8] M.K. Nazeeruddin, E. Baranoff, M. Grätzel, Dye-sensitized solar cells a brief overview, Sol. Energy 85 (2011) 1172–1178.
[9] Y. Qin, Q. Peng, Ruthenium sensitizers and their applications in dye-sensitized solar cells, Int. J. Photoenergy (2012) 291–579.
[10] N. Tomar, A. Agrawal, V.S. Dhaka, P.K. Suroli, Ruthenium complexes based dye sensitized solar cells: fundamentals and research trends, Sol. Energy 207 (2020) 59–76.
[11] S. Aghazada, M.K. Nazeeruddin, Ruthenium complexes as sensitizers in dye-sensitized solar cells, Inorganics 6 (2) (2018) 52, doi:10.3390/inorganics6020052.
[12] A. Monari, X. Assfeld, M. Beley, P.C. Gros, Theoretical study of new ruthenium-based dyes for dye-sensitized solar cells, J. Phys. Chem. A. 115 (15) (2011) 3596–3603.
[13] Y. Xie, Y. Tang, W. Wu, Y. Wang, J. Liu, X. Li, H. Tian, W.H. Zhu, Porphyrin cosensitization for a photovoltaic efficiency of 11.5%: a record for non-ruthenium solar cells based on iodine electrolyte, J. Am. Chem. Soc. 137 (44) (2015) 14055–14058.
[14] B.B. Weber, E.C. Constable, C.E. Housecroft, Light harvesting with earth abundant d-block metals: development of sensitizers in dye-sensitized solar cells (DSCs), Coord. Chem. Rev. 257 (2013) 3089–3106.
[15] N. Mariotti, M. Bonomo, L. Fagiolari, N. Barbero, C. Gerbaldi, F. Bella, C. Barolo, Recent advances in eco-friendly and cost-effective materials towards sustainable dye-sensitized solar cells, Green Chem 22 (2020) 7168–7218.
[16] C.E. Housecroft, E.C. Constable, The emergence of copper(I)-based dye sensitized solar cells, Chem. Soc. Rev. 44 (2015) 8386–8398.
[17] O.S. Wenger, Is iron the new ruthenium? Chem. Eur. J. 25 (2019) 6043–6052.
[18] M. Yahya, A. Bouziani, C. Ocak, Z. Seferoğlu, M. Sillanpää, Organic/metal-organic photosensitizers for dye-sensitized solar cells (DSSC): recent developments, new trends, and future perceptions, Dyes Pigm. 192 (2021) 109–227.
[19] S. Karthikeyan, J.Y. Lee, Zinc-porphyrin based dyes for dye-sensitized solar cells, J. Phys. Chem. A. 117 (42) (2013) 10973–10979.
[20] M. Urbani, M. Grätzel, M.K. Nazeeruddin, T. Torres, Meso-substituted porphyrins for dye-sensitized solar cells, Chem. Rev. 114 (24) (2014) 12330–12396.
[21] F. Hajizadeh, A.R. Vanani, Y.T. Azar, Theoretical design of Zn-dithiaporphyrins as sensitizer for dye-sensitized solar cells, Curr. Appl. Phys. 18 (10) (2018) 1122–1133.
[22] C.L. Flores, E. Schott, F.C. Cadiz, X. Zarate, Energy conversion process of substituted phthalocyanines with potential application to DSSC: a theoretical study, Theor. Chem. Acc. 137 (4) (2018) 52, doi:10.1007/s00214-018-2229-9.
[23] T. Keawin, R. Tarsang, K. Sirithip, N. Prachumrak, T. Sudyoadsuk, S. Namuangruk, J. Roncali, N. Kungwan, V. Promarak, S. Jungsuttiwong, Anchoring number-performance relationship of zinc-porphyrin sensitizers for dye-sensitized solar cells: a combined experimental and theoretical study, Dyes Pigm. 136 (2017) 697–706.
[24] M. Muddassir, A. Alarifi, N.A.Y. Abduh, M. Afzal, New isomeric pyridyl imine zinc(II) complexes as potential co-sensitizers for state of the Art N719 dye in DSSC, J. Mol. Struct. 1246 (2021) 131191.
[25] J.B. Lopez, N.F. Holguin, 1.J.C. Gonzalez, J.A. Sanchez, D.G. Mitnik, Theoretical study of copper complexes: molecular structure, properties, and its application to solar cells, Int. J. Photoenergy. (013) (2013) 613064.
[26] J. Conradie, Polypyridyl copper complexes as dye sensitizer and redox mediator for dye-sensitized solar cells, Electrochem. Commu. 134 (2022) 107–182.
[27] A. Colombo, C. Dragonetti, D. Roberto, A. Valore, P. Biagini, F. Melchiorre, A simple copper(I) complex and its application in efficient dye sensitized solar cells, Inorg Chim Acta 407 (2013) 204–209.
[28] I. Benesperi, R. Singh, M. Freitag, Copper, coordination complexes for energy-relevant applications, Energies 13 (9) (2020) 2198.
[29] S. Çakar, M. Özacar, The effect of iron complexes of quercetin on dye-sensitized solar cell efficiency, J. Photochem. Photobiol. A: Chem. 346 (2017) 512–522.
[30] E. Jakubikova, D.N. Bowman, Fe(II)-polypyridines as chromophores in dye-sensitized solar cells: a computational perspective, Acc. Chem. Res. 48 (5) (2015) 1441–1449.
[31] T. Duchanois, L. Liu, M. Pastore, A. Monari, C. Cebrián, Y. Trolez, M. Darari, K. Magra, A.F. Monerris, E. Domenichini, M. Beley, X. Assfeld, S. Haacke, P.C. Gros, NHC-based iron sensitizers for DSSCs, Inorganics 6 (2) (2018) 63, doi:10.3390/inorganics6020063.
[32] S. Mukherjee, D.N. Bowman, E. Jakubikova, Cyclometalated Fe (II) complexes as sensitizers in dye-sensitized solar cells, Inorg. Chem. 54 (2) (2015) 560–569.
[33] T. Jiang, Y. Bai, P. Zhang, Q. Han, D.B. Mitzi, M.J. Therien, Electronic structure and photophysics of a supramolecular iron complex having a long MLCT-state lifetime and panchromatic absorption, Proc. Natl. Acad. Sci. U.S.A. 117 (34) (2020) 20430–20437.
[34] L. Lindh, O. Gordivska, S. Persson, H. Michaels, H. Fan, P. Chábera, N.W. Rosemann, A.K. Gupta, I. Benesperi, J. Uhlig, O. Prakash, E. Sheibani, K.S. Kjaer, G. Boschloo, A. Yartsev, M. Freitag, R. Lomoth, P. Persson, K. Wärnmark, Dye-sensitized solar cells based on Fe N-heterocyclic carbene photosensitizers with improved rod-like push-pull functionality, Chem. Sci. 12 (2021) 16035–16053.
[35] J.H. Yum, E. Baranoff, F. Kessler, A cobalt complex redox shuttle for dye-sensitized solar cells with high open-circuit potentials, Nat. Commun. 3 (1) (2012) 631, doi:10.1038/ncomms1655.
[36] F. Bella, S. Galliano, C. Gerbaldi, G. Viscardi, Cobalt-based electrolytes for dye-sensitized solar cells: recent advances towards stable devices, Energies 9 (5) (2016) 384, doi:10.3390/en9050384.
[37] K.B. Aribia, T. Moehl, S.M. Zakeeruddin, M. Grätzel, Tridentate cobalt complexes as alternative redox couples for high-efficiency dye-sensitized solar cells, Chem. Sci. 4 (2013) 454–459.
[38] M.K. Kashif, J.C. Axelson, N.W. Duffy, C.M. Forsyth, C.J. Chang, J.R. Long, L. Spiccia, U. Bach, A New Direction in Dye-Sensitized Solar Cells Redox Mediator Development: in Situ Fine-Tuning of the Cobalt(II)/(III) redox potential through lewis base interactions, J. Am. Chem. Soc. 134 (40) (2012) 16646–16653.

[39] A.B.M. Garcıa, I. Benesperi, G. Boschloo, J.J. Concepcion, J.H. Delcamp, E.A. Gibson, G.J. Meyer, M. Pavone, H. Pettersson, A. Hagfeldt, M. Freitag, Dye-sensitized solar cells strike back, Chem. Soc. Rev. 50 (2021) 12450.

[40] N. Goswami, P.K. Gogoi, U. Saha, M.K. Bhattacharyya, T.R. Chetia, Synthesis, crystal structure and application of new Cobalt(II) complex [Co(bpy)2NO3]•NO3•5H2O as sensitizer in dye-sensitized solar cells, Asian J. Chem. 30 (2018) 679–683.

[41] S. Wahyuningsih, A.H. Ramelan, I. Badriyah, I.O. Kristy, N.S. Dewi, S.B. Rahardjo "Third row metal complexes as an alternative dye in dye sensitized solar cell system", Proc. SPIE 8830, Organic Photovoltaics XIV, 88302F (2013) https://doi.org/10.1117/12.2025228.

[42] S. Matsunaga, Thematic issue: cobalt catalysis, Beilstein J. Org. Chem. (2018) 14. https://www.beilstein-journals.org/bjoc/series/86

[43] L. Alig, M. Fritz, S. Schneider, First-row transition metal (De)hydrogenation catalysis based on functional pincer ligands, Chem. Rev. 119 (4) (2019) 2681–2751.

[44] Eds Cobalt Catalysis in Organic Synthesis: Methods and ReactionsWiley-VCH Verlag GmbH & Co, M. Hapke, G. Hilt (Eds.) KGaA, 2020. Pages 462, DOI, doi:10.1002/9783527814855.

[45] N.V. Kulkarni, W.D. Jones, Chemistry of Mn and Co Pincer Compounds in Pincer Compounds Chemistry and Applications, Ed. David Morales-Morales, 2018 Pages 491-518.

[46] M.R. Elsby, R.T. Baker, Strategies and mechanisms of metal-ligand cooperativity in first-row transition metal complex catalysts, Chem. Soc. Rev. 49 (24) (2020) 8933–8987.

[47] W. Liu, B. Sahoo, K. Junge, M. Beller, Cobalt complexes as an emerging class of catalysts for homogeneous hydrogenations, Acc. Chem. Res. 51 (8) (2018) 1858–1869.

[48] Y.-.H. Wang, B. Mondal, S.S. Stah, Molecular cobalt catalysts for O2 reduction to H2O2: benchmarking catalyst performance via Rate-Overpotential Correlations, ACS Catal 10 (20) (2020) 12031–12039.

[49] A.I. Vogel, A Text book of Quantitative Inorganic Analysis, London, Longmans Green and Co. Ltd., 1961 3rd Edn.

[50] A.S. Potapov, A.I. Khlebnikov, Synthesis of mixed-ligand copper(II) complexes containing bis(pyrazol-1-yl)methane ligands, Polyhedron 25 (2006) 2683–2690.

[51] S. Swathi, H. Chandran, G. Reshma, S. Nakul, M. Kumar, M.A. Krishnan, N.V. Kulkarni, D. Senthurpandi, S.S. Contractor, S.B. Arakera, First row transition metal complexes of bis(3,5-dimethyl pyrazolyl)methane: synthesis, molecular structure and antibacterial properties, J. Molec. Struct. 1251 (2022) 132018.

[52] A. Binobaid, M. Iglesias, D.J. Beetstra, B. Kariuki, A. Dervisi, I.A. Fallis, K.J. Cavell, Expanded ring and functionalised expanded ring N-heterocyclic carbenes as ligands in catalysis, Dalton Trans (2009) 7099–7112.

[53] K. Yadav, S. Varshney, A.K. Varshney, Synthesis, characterization and antimicrobial studies of some new organosilicon (IV) complexes with semicarbazones and thio semicarbazones, J. Appl. Chem. 5 (5) (2016) 1097–1104.

[54] M.A. Pasha, M.B. Madhusudana Reddy, Efficient method of synthesis of N,N′-disubstituted ureas/thioureas by a zinc chloride catalyzed thermal reaction, Synth. Commun. 39 (2009) 2928–2934.

[55] G. Reshma, V. Padmanabhan, A.R. Varma, M.S. Gouri, U.R. Nair, P.B. Parvathy, N.V. Kulkarni, D. Senthurpandi, Synthesis and structure of mono and bis {1,3-bis(2-pyridylimino)isoindoline} supported 3d transition metal complexes, J. Mol. Struct. 1226 (2021) 129344.

[56] A. Hille, I. Ott, A. Kitanovic, I. Kitanovic, H. Alborzinia, E. Lederer, S. Wolfl, N. Metzler-Nolte, S. Schafer, W.S. Sheldrick, C. Bischof, U. Schatzschneider, R. Gust, [N,N'-Bis(salicylidene)-1,2-phenylenediamine]metal complexes with cell death promoting properties, J. Biol. Inorg. Chem. 14 (2009) 711–725.

[57] S.V. Samuelsen, C. Santilli, M.S.G. Ahlquist, R. Madsen, Development and mechanistic investigation of the manganese(III) salen-catalyzed dehydrogenation of alcohols, Chem. Sci. 10 (2019) 1150–1157.

[58] K. Cheng, Q.-.Z. Zheng, Y. Qian, L. Shi, J. Zhao, H.-.L. Zhu, Synthesis, antibacterial activities and molecular docking studies of peptide and Schiff bases as targeted antibiotics, Bioorg. Med. Chem. 17 (2009) 7861–7871.

[59] M. Sahin, N. Kocak, U. Arslan, O. Sahin, M. Yilmaz, Bis-schiff base derivatives of 2,5-dihydroxybenzaldehyde: synthesis, characterization and antimicrobial activity of their Cu(II), Co(II) and Zn(II) complexes, J. Macromol. Sci. A 50 (2013) 821–827.

[60] E. Lamour, S. Routier, J.-.L. Bernier, J.-.P. Catteau, C. Bailly, H. Vezin, Oxidation of CuII to CuIII, free radical production, and DNA cleavage by hydroxy-salen−copper complexes. isomeric effects studied by ESR and electrochemistry, J. Am. Chem. Soc. 121 (9) (1999) 1862–1869.

[61] A.I. Vogel, A Text Book of Practical Organic Chemistry, 3rd ed., Longmans, (1973) Page 345.

[62] K. Shimayama, M.R. Karim, S.A. Amolegbe, M. Nakaya, M. Nakamura, R. Ohtani, L.F. Lndoy, S. Hayami, Photoswitching of the dielectric property of salicylideneaniline, J. Incl. Phenom. Macrocycl. Chem. 82 (2015) 219–223.

[63] A.M.A. Belal, M.A. Zayed, M. El-Desawy, S.M.A.H. Rakha, Structure investigation of three hydrazones Schiff's bases by spectroscopic, thermal and molecular orbital calculations and their biological activities, Spectrochim. Acta. 138 (2015) 49–57.

[64] J. Yang, J. Rui, X. Xu, Y. Yang, J. Su, H. Xu, Y. Wang, N. Sun, S. Wang, Fluorescence staining of salicylaldehyde azine, and applications in the determination of potassium tert-butoxide, RSC Adv 6 (2016) 30636–30641.

[65] G.S. Mrđan, G.G. Vastag, D.D. Škorić, M.M. Radanović, T.Ž. Verbić, M.K. Milčić, I.N. Stojiljković, O.S. Marković, B.M. Matijević, Synthesis, physicochemical characterization, and TD-DFT calculations of monothiocarbohydrazone derivatives, Struct. Chem. 32 (2021) 1231–1245.

[66] G.R. Burns, Metal complexes of thiocarbohydrazide, Inorg. Chem. 7 (1968) 277–283.

[67] K.H.M.E. Tehrani, F. Kobarfarda, P. Azerang, M. Mehravar, Z. Soleimania, G. Ghavamic, S. Sardaric, Synthesis and antimycobacterial activity of symmetric thiocarbohydrazone derivatives against mycobacterium bovis BCG, Iran J. Pharm. Res. 12 (2) (2013) 331–346.

[68] L. Li, T.Y. Zhai, Y. Bando, D. Golberg, Recent progress of one-dimensional ZnO nanostructured solar cells, Nano Energy 1 (2012) 91–106.

[69] V. Hegde, T.S. Nivin, S.D. Baby Sreeja, S. Gopalan, C.O. Sreekala, Photovoltaic studies of hybrid metal oxide semiconductors as photo anode in dye sensitized solar cells, AIP Conference Proceedings 2162 (2019) 020129, doi:10.1063/1.5130339.

[70] H. Shahroosvand, L. Najafi, L. Khanmirzaei, S. Tarighi, Artificial photosynthesis based on ruthenium(II) tetrazole-dye-sensitized nanocrystalline TiO2 solar cells, J. Photochem. Photobiol. B: Biology 15 (2015) 4–13.

[71] N.F.M. Sharifa, S. Shafiea, M.Z.A.A. Kadird, W.Z.W. Hasana, M.N. Mustafa, B. Samaila, The effect of titanium (IV) chloride surface treatment to enhance charge transport and performance of dye-sensitized solar cell, Result. Phys 15 (2019) 102725.

[72] A. Vasanth, N.S. Powar, D. Krishnan, S.V. Nair, M. Shanmugam, J. Sci-Adv. Mater. Dev. 5 (3) (2020) 316–321.

[73] BrukerSAINT, Bruker AXS Inc, Madison, Wisconsin, USA, 2012.

[74] Bruker (2006). SADABS. Madison, Wisconsin, USA: Bruker AXS Inc.

[75] G.M. Sheldrick, Crystal structure refinement with SHELXL, Acta Cryst 71 (2015) 3–8 C.

[76] C.B. Hubschle, ShelXle: a Qt graphical user interface for SHELXL, J. Appl. Cryst. (2011) 1281–1284.

[77] L.J. Farrugia, WinGX and ORTEP for windows: an update, J. Appl. Cryst. 45 (2012) 849–854.

[78] Website: 2020, https://www.ccdc.cam.ac.uk/Community/csd-community/FreeMercury/

[79] Y. Zhao, D.G. Truhlar, The M06 suite of density functionals for main group thermochemistry, thermochemical kinetics, noncovalent interactions, excited states, and transition elements: two new functionals and systematic testing of four M06-class functionals and 12 other functionals, Theor. Chem. Acc. 120 (2006) 215–241.

[80] A.D. Becke, Density-functional thermochemistry. III. the role of exact exchange, J. Chem. Phys. 98 (1993) 5648–5652.

[81] P.J. Stephens, F.J. Devlin, C.F. Chabalowski, M.J. Frisch, Ab initio calculation of vibrational absorption and circular dichroism spectra using density functional force fields, J. Phys. Chem. 98 (1994) 11623–11627.

[82] M. Dolg, U. Wedlg, H. Stoll, H. Preuss, Energy-adjusted ab initio pseudopotentials for the first row transition elements, J. Chem. Phys. 86 (1987) 866–872.

[83] J.M.L. Martin, A. Sundermann, Correlation consistent valence basis sets for use with the stuttgart-dresden-bonn relativistic effective core potentials: the atoms Ga-Kr and In-Xe, J. Chem. Phys. 114 (2001) 3408–3420.

[84] Gaussian 16, Revision C.01, M.J. Frisch, G.W. Trucks, H.B. Schlegel, G.E. Scuseria, M.A. Robb, J.R. Cheeseman, G. Scalmani, V. Barone, G.A. Petersson, H. Nakatsuji, X. Li, M. Caricato, A.V. Marenich, J. Bloino, B.G. Janesko, R. Gomperts, B. Mennucci, H.P. Hratchian, J.V. Ortiz, A.F. Izmaylov, J.L. Sonnenberg, D. Williams-Young, F. Ding, F. Lipparini, F. Egidi, J. Goings, B. Peng, A. Petrone, T. Henderson, D. Ranasinghe, V.G. Zakrzewski, J. Gao, N. Rega, G. Zheng, W. Liang, M. Hada, M. Ehara, K. Toyota, R. Fukuda, J. Hasegawa, M. Ishida, T. Nakajima, Y. Honda, O. Kitao, H. Nakai, T. Vreven, K. Throssell, J.A. Montgomery, Jr, J.E. Peralta, F. Ogliaro, M.J. Bearpark, J.J. Heyd, E.N. Brothers, K.N. Kudin, V.N. Staroverov, T.A. Keith, R. Kobayashi, J. Normand, K. Raghavachari, A.P. Rendell, J.C. Burant, S.S. Iyengar, J. Tomasi, M. Cossi, J.M. Millam, M. Klene, C. Adamo, R. Cammi, J.W. Ochterski, R.L. Martin, K. Morokuma, O. Farkas, J.B. Foresman, D.J. Fox, Gaussian, Inc, Wallingford CT (2016).

[85] R.M. Awadallah, Preparation and charecterization of Iron (II, III), Cobalt (II, III) and Nickel (II) complexes of 2,2-Dipyridyl, Asian J. Chem. 6 (2) (1994) 393–404.

[86] J. Bi, L. Kong, Z. Huang, J. Liu, Self-encapsulation of [MII(phen)2(H2O)2]2+ (M = Co, Zn) in one-dimensional nanochannels of [MII(H2O)6(BTC)2]4- (M = Co, Cu, Mn): a high HQ/CAT ratio catalyst for hydroxylation of phenols, Inorg. Chem. 47 (11) (2008) 4564–4569.

[87] K. Yadav, S. Varshney, A.K. Varshney, Synthesis, spectral and antimicrobial investigation of some new coordination compounds of Palladium (II) with biologically active nitrogen donor ligands, Int. J. Pharma. Sci. Rev. Res. 41 (2) (2016) 72–78.

[88] T.V. Koksharova, S.V. Fel'dman, Cobalt(II), Nickel(II), and Copper(II) Complexes with Diphenylthiocarbazide, Russ. J. Coord. Chem. 27 (10) (2001) 738–740.

[89] H. Li, D. Xi, Y. Niu, C. Wang, F. Xu, L. Liang, P. Xu, Design, synthesis and biological evaluation of cobalt(II)-Schiff base complexes as ATP-noncompetitive MEK1 inhibitors, J. Inorg. Biochem. 195 (2019) 174–181.

[90] A. Kumar, G.S. Mishra, A. Kumar, Covalantly bonded Schiff base cobalt complex catalyst for the selective oxidation of linear alkanes using molecular oxygen, J. Molec. Cat. A: Chemical 201 (2003) 179–188.

[91] R.H. Bailes, M. Calvin, The oxygen-carrying synthetic chelate compounds. VII. preparation, J. Am. Chem. Soc. 69 (8) (1947) 1886–1893.

[92] R.C. Aggarwal, N.K. Singh, R.P. Singh, Magnetic and spectroscopic studies on salicylaldoxime and -hydroxynapthaldoxime complexes of some divalent 3d metal ions, Synth. React. Inorg. Met.-Org. Chem. 14 (5) (1984) 637–650.

[93] W. Rehman, F. Saman, I. Ahmad, Synthesis, characterization, and biological study of some biologically potent schiff base transition metal complexes, Russ. J. Coord. Chem. 34 (9) (2008) 678–682.
[94] R.C. Aggarwal, N.K. Singh, R.P. Singh, Synthesis and structural studies of first row transition metal complexes of salicylaldehyde hydrazone, Inorg. Chim. Acta 32 (2) (1979) L87–L90.
[95] M. Salavati-Niasari, A. Amiri, Synthesis and characterization of alumina-supported Mn(II), Co(II), Ni(II) and Cu(II) complexes of bis(salicylaldiminato)hydrazone as catalysts for oxidation of cyclohexene with tert-buthylhydroperoxide, Appl. Cataly. A 290 (2005) 46–53.
[96] M.S. Raizada, H.L. Nigam, M.N. Srivastava, Proceed. Nat. Acad. Sci., India, Section A: Physical Sciences 65 (2) (1995) 165–172.
[97] N.V. Kulkarni, A. Kamath, S. Budagumpi, V.K. Revankar, Pyrazole bridged binuclear transition metal complexes: synthesis, characterization, antimicrobial activity and DNA binding/cleavage studies, J. Mol. Struct. 1006 (2011) 580–588.
[98] W.J. Geary, The use of conductivity measurements in organic solvents for the characterisation of coordination compounds, Coord. Chem. Rev. 7 (1971) 81–122.
[99] M. Viswanathan, Synthesis and elucidation of some mixed ligand complexes of Th(IV) with N-(1-morpholinobenzyl) semicarbazide, Asian J. Chem. 28 (6) (2016) 1221–1224.
[100] N.V. Kulkarni, V.K. Revankar, B.N. Kirasur, M.H. Hugar, Transition metal complexes of thiosemicarbazones with quinoxaline hub: an emphasis on antidiabetic property, Med. Chem. Res. 21 (2012) 663–671.
[101] G. Reshma, S. Nakul, P.M. Mahitha, N.V. Kulkarni, D. Senthurpandi, S.R.K.C.S. Yamijala, W.W. Brennessel, W.D. Jones, Synthesis and molecular structure of half- sandwich ruthenium (II) complexes containing pyrazolyl ligands, J. Mol. Struct. 1251 (2022) 132005.
[102] C. Hemmert, M. Renz, H. Gornitzka, S. Soulet, B. Meunier, Preparation and crystal structures of manganese, iron, and cobalt complexes of the Bis[*di*(2-*pyridyl*)*methyl*]amine (bdpma) Ligand and its oxidative degradation product 1,3,3 Tris(2-pyridyl)-3H-imidazo[1,5-*a*]pyridin-4-ium (tpip); origin of the bdpma fragility, Chem. Eur. J. 5 (6) (1999) 1766–1774.
[103] K.K. Chenab, B. Sohrabi, M.R.Z. Meymian, Cobalt complex dye as a novel sensitizer in dye sensitized solar cells, Mater. Res. Express. 6 (2019) 125536.
[104] J. Massin, L. Ducasse, M. Abbas, L. Hirsch, T. Toupance, C. Olivier, Molecular engineering of carbazole-fluorene sensitizers for high open-circuit voltage DSSCs: synthesis and performance comparison with iodine and cobalt electrolytes, Dyes Pigm 118 (2015) 76–87.
[105] J. Tauc, Optical properties and electronic structure of amorphous Ge and Si, Mater. Res. Bull. 3 (1968) 37–46.
[106] K.J. Hamam, M.I. Alomari, A study of the optical band gap of zinc phthalocyanine nanoparticles using UV–Vis spectroscopy and DFT function, Appl. Nanosci. 7 (2017) 261–268.
[107] N.V. Kulkarni, G.S. Hegde, G.S. Kurdekar, S. Budagumpi, M.P. Sathisha, V.K. Revankar, Spectroscopy, electrochemistry, and structure of 3d-transition metal complexes of thiosemicarbazones with quinoline core: evaluation of antimicrobial property, Spectrosc. Lett 43 (2010) 235–246.
[108] L. Sacconi, M. Ciampolini, G.P. Speroni, High-spin hexa-, penta-, and tetracoordinated complexes of cobalt (II) with schiff bases formed from salicylaldehydes and N, N- substituted ethylenediamines, Inorg. Chem. 4 (8) (1965) 1116–1119.
[109] N.V. Kulkarni, N.H. Bevinahalli, V.K. Revankar, J. Coord. Chem. 63 (10) (2010) 1785–1794.
[110] S.K. Padhi, R. Sahu, Co(II/III) coordinated pyridine alcoholate ligand generated through metal assisted nucleophilic addition to a C=O function: temperature dependent synthesis of a mononuclear complex and a neutral cubane cluster, Polyhedron 27 (2008) 2662–2666.
[111] B. Machura, J.G. Małecki, A. Świtlicka, I. Nawrot, R. Kruszynski, Copper (II) complexes of bis(pyrazol-1-yl) methane - Synthesis, spectroscopic characterization, X-ray structure and DFT calculations, Polyhedron 30 (2011) 864–872.
[112] S.O. Sommerer, J.D. Baker, W.P. Jensen, A. Hamza, R.A. Jacobson, The X-ray structure analysis of bis-2,2′,N,N′-bipyridyl ketone cobalt (III) nitrate dihydrate, Inorg. Chim. Acta. 210 (1993) 173–176.
[113] W.P. Jensen, A.I. Hamza, I.H. Suh, R.A. Jacobson, S.O. Sommerer, The crystal and molecular structure of [2, 2′-N, N′-O-bipyridylketonehydrate, N, N-bipyridylketone oxime nitro cobalt (III) dihydrate], Inorg. Chim. Acta. 254 (1997) 367–370.
[114] I.J. Bakker, M.C. Feller, R. Robson, Complexes of di-2-pyridylketone—III: some chelated products of metal-promoted hydration of the ketone, J. Inorg, Nucl. Chem 33 (1971) 747–754.
[115] M.L. Tong, G. Yang, X.M. Chen, S.W. Ng, Bis[*di*-2-*pyridylmethanediolato*(1-)-N, O, N']cobalt(III) Perchlorate Trihydrate, Acta Cryst 54 (1998) 217–219 C.
[116] G. Crundwell, B.L. Westcott, R. Coffey, M. Zeller, A.D. Hunter, Crystal structures of two different cobalt(III) complexes with di-2-pyridyl ketone grown from methanol-bis-(methoxy-bis(2-pyridyl)methanolato-O,N,N') -cobalt(III) nitrate trihydrate and (hydroxy-bis(2-pyridyl)methanolato-O,N,N')-(methoxy-bis(2-pyridyl)methanolato-O,N,N ')-cobalt(III) nitrate trihydrate, Inorg. Chim. Acta 355 (2003) 432–437.
[117] J.L. Bredas, Mind the gap! Mater, Horiz 1 (2014) 17–19.
[118] Peter I. Djurovich, Elizabeth I. Mayo, Stephen R. Forrest, Mark E. Thompson, Measurement of the lowest unoccupied molecular orbital energies of molecular organic semiconductors, Org. Electronics 10 (2009) 515–520.
[119] Y.C. Hung, J.C. Jiang, C.Y. Chao, W.F. Su, S.T. Lin, Theoretical study on the correlation between band gap, bandwidth, and oscillator, strength in fluorene-based donor-acceptor conjugated copolymers, J. Phys. Chem. B 113 (2009) 8268–8277.
[120] M. Karuppusamy, V.S.K. Choutipalli, D. Vijay V Subramanian, Rational design of novel N-doped polyaromatic hydrocarbons as donors for the perylene based dye-sensitized solar cells, J. Chem. Sci. 132 (2020) 20. https://doi.org/10.1007/s12039-019-1723-5Sadhana (0123456789-volV) [FT3] (0123456)
[121] L. Leonat, G. Sbarcea, I.V. Branzoi, Cyclic voltammetry for energy levels estimation of organic materials, U. P. B Sci. Bull. Ser. B 1 (2013) 111–118.
[122] G.A. Mathew, M.R.N. Munichandraiah, Effect of TiO2 electrode thickness on photovoltaic properties of dye sensitized solar cell based on randomly oriented Titania nanotubes, Materials Chem. Phy. 127 (1–2) (2011) 95–101.
[123] J.M.K.W. Kumari, N. Sanjeevadharshini, M.A.K.L. Dissanayake, G.K.R. Senadeera, C.A. Thotawatthage, The effect of TiO2 photoanode film thickness on photovoltaic properties of dye-sensitized solar cells, Ceylon. J. Sci. 45 (1) (2016) 33–41.
[124] S. Challagulla, K. Tarafder, R. Ganesan, S. Roy, Structure sensitive photocatalytic reduction of nitroarenes over TiO2, Sci. Rep. 7 (2017) 8783.
[125] W. Su, J. Zhang, Z. Feng, T. Chen, P. Ying, C. Li, Surface phases of TiO2 nanoparticles studied by UV raman spectroscopy and FT-IR spectroscopy, J. Phys. Chem. C 112 (20) (2008) 7710–7716.
[126] S. Nagai, G.H.T. Bessho, K. Satori, Raman spectroscopic study of dye adsorption on TiO2 electrodes of dye-sensitized solar cells, Vib. Spectrosc. 72 (2014) 66–71.
[127] K.E. Lee, M.A. Gomez, S. Elouatik, G.P. Demopoulos, Further understanding of the adsorption mechanism of N719 sensitizer on anatase TiO2 films for DSSC applications using vibrational spectroscopy and confocal raman imaging, Langmuir 26 (12) (2010) 9575–9583.
[128] U. Würfel, D. Neher, A. Spies, S. Albrecht, Impact of charge transport on current-voltage characteristics and power-conversion efficiency of organic solar cells, Nat. Commun. 6 (2015) 6951, doi:10.1038/ncomms7951.